

ALMA Polarization Study of the Magnetic Fields in Two Massive Clumps in the 20 km s⁻¹ Cloud of the Central Molecular Zone

YUHUA LIU (柳玉华),¹ XING LU (吕行),^{1,2} JUNHAO LIU (刘峻豪),³ XING PAN (潘兴),^{4,5,6} QIZHOU ZHANG,⁶ HAYU BAOBAB LIU,^{7,8} MENG-ZHE YANG,⁹ SHIH-PING LAI,⁹ TAO-CHUNG CHING,¹⁰ WENYU JIAO (焦文裕),¹ YANKUN ZHANG (张燕坤),¹ PAK SHING LI,¹ ZHIQIANG SHEN (沈志强),^{1,2} TIE LIU (刘铁),^{1,2} ADAM GINSBURG,¹¹ QI-LAO GU (顾琦烙),¹ AND MENGKE ZHAO^{12,4}

¹Shanghai Astronomical Observatory, Chinese Academy of Sciences, 80 Nandan Road, Shanghai 200030, P. R. China

²State Key Laboratory of Radio Astronomy and Technology, A20 Datun Road, Chaoyang District, Beijing, 100101, P. R. China

³National Astronomical Observatory of Japan, 2-21-1 Osawa, Mitaka, Tokyo, 181-8588, Japan

⁴School of Astronomy and Space Science, Nanjing University, 163 Xianlin Avenue, Nanjing 210023, P. R. China

⁵Key Laboratory of Modern Astronomy and Astrophysics (Nanjing University), Ministry of Education, Nanjing 210023, P.R.China

⁶Center for Astrophysics | Harvard & Smithsonian, 60 Garden Street, Cambridge, MA, 02138, USA

⁷Department of Physics, National Sun Yat-Sen University, No. 70, Lien-Hai Road, Kaohsiung City 80424

⁸Center of Astronomy and Gravitation, National Taiwan Normal University, Taipei 116

⁹Institute of Astronomy and Department of Physics, National Tsing Hua University, Hsinchu 30013, Taiwan

¹⁰National Radio Astronomy Observatory, P.O. Box O, Socorro, NM 87801, USA

¹¹University of Florida Department of Astronomy, Bryant Space Science Center, Gainesville, FL, 32611, USA

¹²South-Western Institute for Astronomy Research, Yunnan University, Chenggong District, Kunming 650500, China

ABSTRACT

We present the Atacama Large Millimeter/submillimeter Array (ALMA) observations of linearly polarized 870 μ m continuum emission at a resolution of \sim 0.⁰2 (2000 au) toward the two massive clumps, Clump 1 and Clump 4, in the 20 km s⁻¹ cloud. The derived magnetic field strengths for both clumps range from \sim 0.3 to 3.1 mG using the Angular Dispersion Function (ADF) method. The magnetic field orientations across multiple scales suggest that the magnetic field dominates at the cloud scale, whereas gravity likely governs structures at the core (0.01–0.1 pc) and condensation (\leq 0.01 pc) scales. Furthermore, the study on the angular difference between the orientations of the local gravity gradient and the magnetic field suggests that the magnetic field predominantly governs the dynamics in the diffuse regions, while gravity and star formation feedback become increasingly significant within the dense regions. The ratio of the magnetic field tension force F_B to the gravitational force F_G suggests that the magnetic field may provide some support against gravity, but it is insufficient to prevent gas from infalling toward the dense cores.

Keywords: Interstellar magnetic fields (845); Polarimetry (1278); Galactic center (565)

1. INTRODUCTION

The central molecular zone (CMZ; M. Morris & E. Serabyn 1996) is the innermost region of the Milky Way with a Galactocentric radius of \sim 300 pc (J. D. Henshaw et al. 2023). This region contains a large amount of molecular gas of \gtrsim 10⁷ M_⊙ (e.g., G. Dahmen et al. 1998; S. N. Longmore et al. 2013; C. Battersby et al. 2024), and represents a star-forming environment under some extreme physical conditions. The magnitudes of the av-

erage number density of molecular gas (\gtrsim 10⁴ cm⁻³; e.g., J. Bally et al. 1987; K. Ferrière et al. 2007; S. N. Longmore et al. 2013), gas temperatures (\sim 25 K to $>$ 100 K; e.g., Y. Ao et al. 2013; A. Ginsburg et al. 2016; K. Immer et al. 2016; N. Krieger et al. 2017), Mach numbers (10–20; e.g., C. Federrath et al. 2016; J. D. Henshaw et al. 2016), and magnetic field strengths (\sim 0.1 mG to \gtrsim 1 mG; e.g., T. Pillai et al. 2015; A. Mangilli et al. 2019; X. Lu et al. 2024; X. Pan et al. 2024, 2025; D. M. Paré et al. 2025) in this region are found to be higher than those in the Galactic disk. However, the star formation rate (SFR) is about one order of magnitude lower than expected, considering the mass and density of the dense

gas in this region (e.g., S. N. Longmore et al. 2013; A. T. Barnes et al. 2017).

Observations have identified several massive molecular clouds within the CMZ, such as G0.253+0.016, the 20 km s⁻¹ cloud, the 50 km s⁻¹ cloud, Sgr C, and Sgr B2 (e.g., J. Kauffmann et al. 2017). Some of these clouds except for Sgr B2 have shown lower SFRs than predicted by the dense gas star formation relation derived from the solar neighborhood (e.g., J. Kauffmann et al. 2017; X. Lu et al. 2019a). J. M. D. Kruijssen et al. (2014) suggested that the low star SFR in the CMZ is primarily due to the strong turbulence. Later, X. Lu et al. (2024) emphasized that turbulence and self-gravity play the important roles in star formation based on the observed weak correlation between magnetic field strength and SFR. More recently, M.-Z. Yang et al. (2025) indicated that weak correlation between magnetic field strength and SFR could imply that the SFR is not linearly correlated with magnetic field strength and suggested that the dominance of magnetic fields may also play a crucial role in suppressing the star formation in this region. Furthermore, X. Pan et al. (2025) presented a SOFIA data for the CMZ revealed a parallel configuration of the relative orientation between the magnetic field and column density and a supervirial state for all CMZ clouds except for Sgr B2, suggesting that self-gravity may not be dominant even in the most dense structures. The role of the magnetic field and in particular its interplay with other sources such as gravity in star formation remains unclear. All above studies were conducted at spatial resolutions of 0.2–0.5 pc. To address this degeneracy, we present high-resolution polarization observations that trace magnetic field morphology at an unprecedented resolution of \sim 0.01 pc (2000 au).

In this work, we study the magnetic field properties and morphologies through the Atacama Large Millimeter/submillimeter Array (ALMA) high angular resolution polarization observations toward two massive clumps, named as Clump 1 and Clump 4, in the 20 km s⁻¹ cloud (see Figure 1(a)), one of the massive molecular clouds ($\gtrsim 10^5 M_\odot$; X. Lu et al. 2015, 2017) in the CMZ, which is highly turbulent and also relatively more active in star formation compared to the other clouds (J. Kauffmann et al. 2017; X. Lu et al. 2019b). We aim to characterize the magnetic field properties toward this cloud.

2. OBSERVATIONS AND DATA REDUCTION

2.1. ALMA observations

The ALMA Band 7 (870 μ m) full polarization observations targeting seven fields in the CMZ, among which four fields are inside the 20 km s⁻¹ cloud (see the lime

circles in Figure 1(a)), were obtained in Cycle 8 (Project ID: 2021.1.00286.S; PI: X. Lu) using two array configurations. The higher resolution observations ($\sim 0.^{\prime\prime}24 \times 0.^{\prime\prime}16$) were obtained on 2022 June 15 and 16 in two consecutive observing blocks, using the more extended C-5 configuration with a projected baseline range of 15 m to 1.3 km. The lower resolution observations ($\sim 0.^{\prime\prime}71 \times 0.^{\prime\prime}54$) were obtained on 2022 April 10 in one observing block, using the compact C-2 configuration with a projected baseline range of 15 to 455 m. The on-source time for each field in the C-5 and C-2 configurations is 114 and 30 minutes, respectively. Between 44 and 48 of the 12-m antennas were operated during the observations. The full width at half maximum (FWHM) of the ALMA primary beam is $\sim 17.^{\prime\prime}$. The maximum recoverable size is $\sim 6.1.^{\prime\prime}$. Four spectral windows (SPWs) centered at 334.2, 336.1, 346.2, and 348.1 GHz, each with a total bandwidth of 1.875 GHz, were allocated with the frequency division mode for the continuum observations. The raw data were first calibrated with the standard ALMA pipeline using the Common Astronomy Software Applications (CASA; CASA Team et al. 2022) version 6.2.1-7, followed by polarization calibrations done by a customized calibration script provided by the ALMA staff.

Furthermore, two additional executions in the C-2 configuration were obtained on 2022 March 31, with the baselines ranging from 14 to 313 m. The data are labeled as Quality Assurance (QA) semipass due to a phase loop lock (PLL) error of ALMA. As described in X. Lu et al. (2026, in preparation), the outcomes of the QA-pass and QA-semipass data are consistent, hence the QA-semipass data were incorporated in the final imaging to improve the continuum sensitivity.

We began by inspecting the calibrated data and flagging channels with line contamination. Then, the flagged data from the two array configurations, including the QA-semipass data for each field C20_c1a, C20_c1b, C20_c4a, and C20_c4b (see Figure 1(a)) were combined using the CASA task `concat`. In order to enhance the image quality for Stokes I , we performed three rounds of phase self-calibration. We derived the self-calibration solutions to each field separately. The first round of self-calibration was derived with a solution interval equivalent to the scan length (\sim 60 s). The second and third rounds were derived with the solution intervals equal to the integration time (\sim 6 s). Then, we combined the fields C20_c1a and C20_c1b, as well as C20_c4a and C20_c4b, to produce mosaicked continuum images for Clump 1 and Clump 4, respectively, as shown in Figures 1(b) and (c). The Stokes I images were made using the data with self-calibration applied,

whereas the Stokes Q and U images were made using the data without self-calibration. The final CLEANed images of Stokes I , Q , and U for each clump were made using the CASA task `tclean` with Briggs weighting (robust = 0.5) and multi-scale algorithm with scales of [0, 5, 15, 50, 150] pixels, each pixel having a size of 0''.04. The debiased linearly polarized intensity (PI) was derived from Stokes Q and U as $\text{PI} = \sqrt{Q^2 + U^2 - \sigma_{QU}^2}$,

where $\sigma_{QU} = \sqrt{\sigma_Q^2 + \sigma_U^2}$. The position angle (P.A.) of the polarization vector $\chi = \frac{1}{2}\arctan(U/Q)$ was computed using the CASA task `immath`. Each of the Stokes I and polarization vector images was obtained using pixels where an emission detection is $\geq 3\sigma_{QU}$.

In order to compare the magnetic field morphology at different scales, we additionally imaged the continuum emission for both Clump 1 and Clump 4 using the extended C-5 and compact C-2 configurations separately. These images were made using the self-calibrated data as described above. Table 1 summarizes the rms noise level measured in each Stokes component, the synthesized beam, and P.A. for each of the continuum images.

In addition to the continuum images, we also imaged each SPW in these datasets to search for possible lines that could trace the turbulence. The HN¹³C ($J = 4-3$) line image will be used to derive the velocity dispersion. The details can be found in Appendix C.

Table 1. Summary of the images

Image Name	rms Noise Level ($\mu\text{Jy beam}^{-1}$)	Synthesized Beam Size ('' \times '')	P.A. (°)	Figure
Clump 1	65, 18, 18	0.31 \times 0.21	81	1 (b)
Clump 4	48, 17, 17	0.31 \times 0.21	81	1 (c)
Clump 1(C-2)	220, 33, 33	0.71 \times 0.54	81	2 (b)
Clump 1(C-5)	32, 21, 21	0.24 \times 0.17	84	2 (c)-(d)
Clump 4(C-2)	210, 33, 33	0.71 \times 0.55	81	3 (b)
Clump 4(C-5)	22, 21, 21	0.24 \times 0.16	84	3 (c)-(h)

2.2. JCMT SCUBA-2/POL-2 Observations

We utilized the data obtained from James Clerk Maxwell Telescope (JCMT) observations toward the 20 km s⁻¹ cloud (M.-Z. Yang et al. 2025; J. Karoly et al. 2025) to compare with the ALMA data in this work. The 850 μm continuum and polarization observations were conducted using the Common-User Bolometer Array 2 (SCUBA-2) with the POL-2 polarimeter on the JCMT as part of the B-fields In STar forming Regions Observations (BISTRO) survey (Project ID: M20AL018; D. Ward-Thompson et al. 2017). The beam size is 14''.6 (J. T. Dempsey et al. 2013). The

SCUBA-2/POL-2 raw data were reduced using the Sub-Millimetre User Reduction Facility (SMURF) package with `pol2map` routine (E. L. Chapin et al. 2013). The details of the data reduction were described by J. Karoly et al. (2025). We obtained the Stokes I, Q, U images from M.-Z. Yang et al. (2025) and the debiased polarization catalog was binned to 12'' (M.-Z. Yang et al. 2025).

3. RESULTS

3.1. 870 μm Dust Continuum (Stokes I)

Figures 1 (b) and (c) show 870 mm continuum emissions for Clump 1 and Clump 4 overlaid with the inferred magnetic field orientations (by rotating the polarization orientation by 90°) assuming that the dust alignment is due to the magnetic field (e.g., R. H. Hildebrand 1988; B. G. Andersson et al. 2015). These two clumps are split into substructures (cores) using the `astrodendro` Python package (E. W. Rosolowsky et al. 2008). Here, a “core” refers to the branch identified by `astrodendro`, and a “condensation” refers to the isolated compact structure within the core. The details for the dendrogram parameters can be found in Appendix A.

We first estimated the physical properties. The gas mass M_{gas} for each core was estimated as

$$M_{\text{gas}} = \Lambda \frac{F_{\nu} d^2}{\kappa_{\nu} B_{\nu}(T)}, \quad (1)$$

where F_{ν} is the total flux density (with primary-beam-corrected) provided by `astrodendro` for all cores (for Clump 1-tail, F_{ν} is manually measured from the Stokes I image using the CASA task `imstat` with the key `[flux]`), $d = 8.277$ kpc is adopted as the distance to the CMZ assuming that the distance to the CMZ is the same as that to the super massive black hole (GRAVITY Collaboration et al. 2022), $\Lambda = 100$ is the gas-to-dust mass ratio, $\kappa_{\nu} = 1.69 \text{ cm}^2 \text{ g}^{-1}$ is the dust opacity interpolated at $\lambda = 870 \mu\text{m}$ from the coagulation model of dust grains coated with thin ice mantles at a gas density of 10^6 cm^{-3} (V. Ossenkopf & T. Henning 1994), $B_{\nu}(T)$ is the Planck function as a function of the dust temperature T . We adopted a uniform dust temperature of $T = 20 \text{ K}$ in the CMZ (D. Pierce-Price et al. 2000; Y. Tang et al. 2021; C. Battersby et al. 2025). The column density N_{H_2} and volume density n_{H_2} were then estimated as

$$N_{\text{H}_2} = \frac{M_{\text{gas}}}{\pi r^2 \mu_{\text{H}_2} m_{\text{H}}}, \quad (2)$$

and

$$n_{\text{H}_2} = \frac{3M_{\text{gas}}}{4\pi r^3 \mu_{\text{H}_2} m_{\text{H}}} = \frac{3N_{\text{H}_2}}{4r}, \quad (3)$$

respectively, where r is the effective radius, $r = \sqrt{A/\pi}$, where A is the exact area of the core, $\mu_{\text{H}_2} = 2.8$ is the

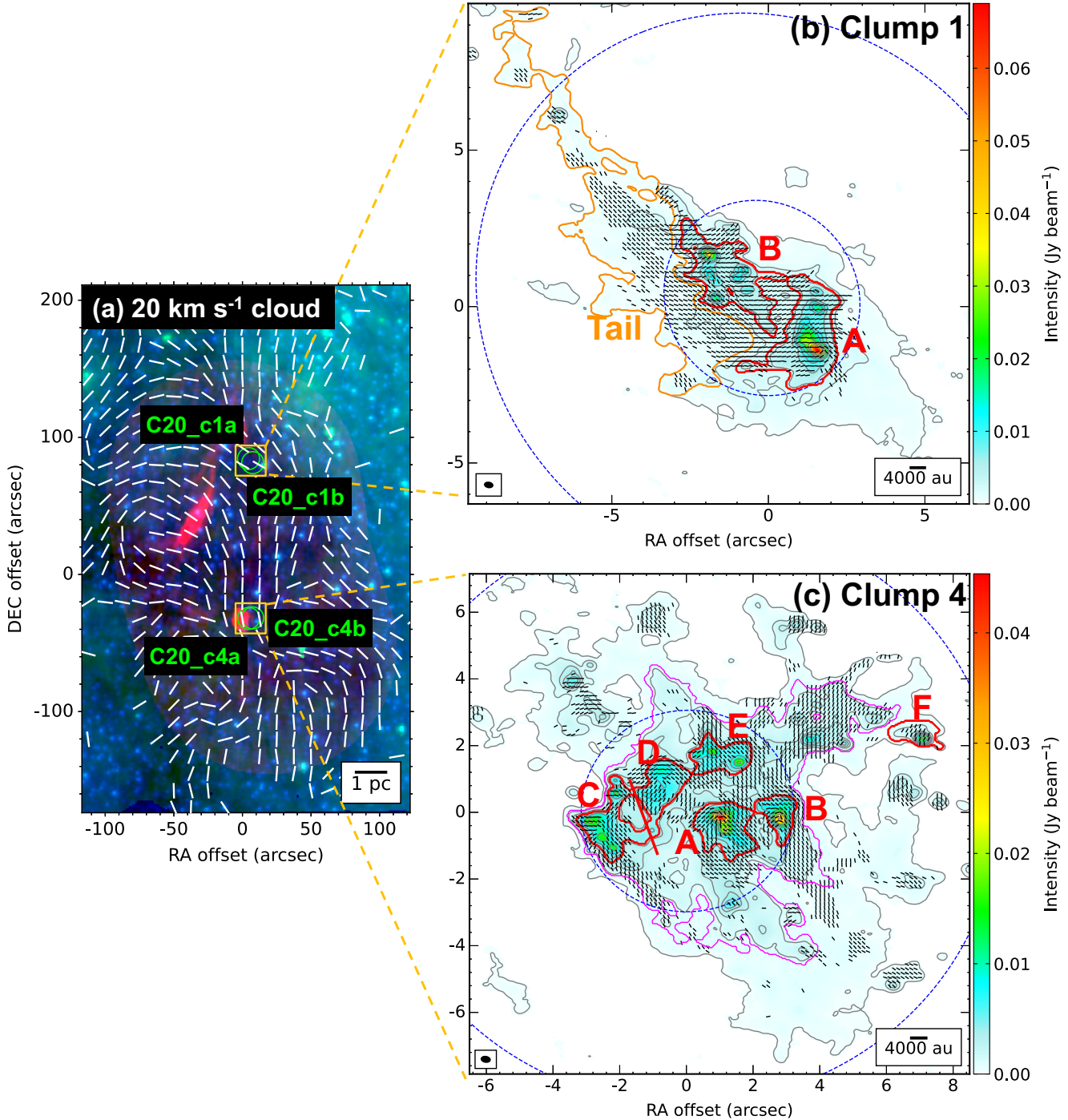


Figure 1. Left: false-color image of the 20 km s^{-1} cloud created using the MeerKAT 1.28 GHz continuum in red (I. Heywood et al. 2022), Spitzer $3.6 \mu\text{m}$ in blue, and Spitzer $8 \mu\text{m}$ in green (S. Stolovy et al. 2006). The white line segments are the inferred magnetic field orientation obtained from James Clerk Maxwell Telescope (JCMT) observations of polarized dust emission (M.-Z. Yang et al. 2025). The ALMA observation fields are denoted by the lime circles. Right: The inferred magnetic field orientation (black line segments) overlaid on Stokes I emission (color) toward (b) Clump 1 and (c) Clump 4. The grey contours are the Stokes I emission, which correspond to $[5, 25, 50, 100, 150, 200, 350, 500, 650] \times \sigma$ ($1\sigma = 65 \mu\text{Jy beam}^{-1}$) in panel (b) and $[5, 25, 50, 75, 100, 150, 250, 350, 450, 650] \times \sigma$ ($1\sigma = 48 \mu\text{Jy beam}^{-1}$) in panel (c). The magenta contour in panel (c) denote the area used to derive the magnetic field properties for Clump 4. The cores enclosed by red solid contours in these two clumps are identified by `astrodendro`. Clump 1-tail is enclosed using the orange solid contour, which is identified as the diffuse emission extended along the northeast-southwest direction that correspond to $\sim 5\sigma$ in panel (b). Clump 4-C and Clump 4-D, identified as one core using `astrodendro`, are manually divided by the red solid line using the 75σ contour as the reference. The synthesized beam size is denoted by filled black ellipse in the bottom left corner. The vectors in all panels are selected using Super-Nyquist sampling (~ 3 pixels per beam; C. L. H. Hull et al. 2020) and set to have a uniform length. The outer and inner blue dashed contours in panels (b) and (c) are the FWHM of the primary beam and the inner $1/3$ of it, respectively. The absolute coordinates of the origins are (a) $[266.408^\circ, -29.0858^\circ]$, (b) $[266.407^\circ, -29.0635^\circ]$, and (c) $[266.407^\circ, -29.0956^\circ]$, respectively.

mean molecular weight per hydrogen molecule (J. Kauffmann et al. 2008), and $m_{\text{H}} = 1.67 \times 10^{-24}$ g is the mass of the hydrogen atom. We assumed a spherical geometry with a volume given by $V = 4/3\pi r^3$. The physical quantities r , F_{ν} , M_{gas} , N_{H_2} , and n_{H_2} are summarized in Table 2.

The gas masses of all cores and Clump 1-tail range from 12 to $240 M_{\odot}$. All the cores show a typical volume density of 10^6 cm^{-3} and a typical column density of 10^{23} cm^{-2} , respectively.

3.2. Magnetic Field Strength

We estimated the plane-of-sky (POS) total magnetic field strengths (B_{pos}) toward Clump 1 and Clump 4 using the Angular Dispersion Function (ADF) method. The ADF method provides estimates of the turbulent-to-ordered magnetic field strength ratio based on the angular dispersion function of the magnetic field position angle, where the angle differences are evaluated as a function of the distance between pairs of points (R. H. Hildebrand et al. 2009; M. Houde et al. 2009, 2016). By using the method developed by R. H. Hildebrand et al. (2009), B_{pos} given by J. Liu et al. (2021, 2022a) is

$$B_{\text{pos}} \sim 0.21 \sqrt{4\pi\rho} \sigma_v \left(\frac{\langle B_{\text{t}}^2 \rangle}{\langle B^2 \rangle} \right)_{\text{int}}^{-\frac{1}{2}}, \quad (4)$$

where $(\langle B_{\text{t}}^2 \rangle / \langle B^2 \rangle)_{\text{int}}^{-1/2}$ is the turbulent-to-total field strength ratio, without correction for line-of-sight (LOS) signal integration. B_{t} denotes the turbulent magnetic field and B denotes the total magnetic field, which the total magnetic field is the sum of the ordered magnetic field and turbulent magnetic field. 0.21 is the average correction factor for the spherical and cylindrical structures (J. Liu et al. 2021). $\rho = n_{\text{H}_2} \mu_{\text{H}_2} m_{\text{H}}$ is the mass density. The turbulent velocity dispersion σ_v is shown in Figure B1. The polarization angle distributions σ_{θ} for the entire Clump 1 and Clump 4 are shown in Figure B2. The polarization angle distributions for the cores within each clump are shown in Figure B3. The ADF is shown in Figure C1. The derivation of $\langle B_{\text{t}}^2 \rangle / \langle B^2 \rangle$ can be found in Appendix C can be found in Appendix C. The cores in Clump 1 have sufficient independent measurements (> 28 ; J. Liu et al. 2021). In Clump 4, however, only the Clump 4-A core has sufficient independent measurements, while all other cores have fewer than 28 independent measurements. Therefore, we only estimated the magnetic field properties for Clump 4-A. In addition, we defined an enclosed area within Clump 4, where polarization detections are concentrated, with more than 70% of all polarization detections above the 5σ level originating there. This selected region was identified by `astrodendro` as a branch included most of the cores

within this clump (enclosed by the magenta contour in Figure 1). The magnetic field properties derived for this enclosed area are taken to represent those of the Clump 4 as a whole.

In this work, we do not use the classical Davis–Chandrasekhar–Fermi (DCF) method to derive the magnetic field strength due to the large angle dispersion in our data especially in Clump 4 as shown in Figure B2 and Figure B3. In addition, the ADF method accounts for the order field and observational effects (e.g., R. H. Hildebrand et al. 2009; M. Houde et al. 2009, 2016) and J. Liu et al. (2021) found that the uncertainty of the ADF method is smaller than DCF.

3.3. Mass-to-flux Ratios

The relative importance of gravity and magnetic fields can be accessed using the mass-to-flux ratio normalized to its critical value, which is described by a dimensionless parameter λ and given by R. M. Crutcher et al. (2004)

$$\lambda = \frac{(M/\Phi)}{(M/\Phi)_{\text{cr}}} = \frac{\pi r^2 \mu_{\text{H}_2} m_{\text{H}} N_{\text{H}_2} / \pi r^2 B_{3\text{D}}}{1/(2\pi\sqrt{G})} = \frac{\mu_{\text{H}_2} m_{\text{H}} N_{\text{H}_2} (2\pi\sqrt{G})}{B_{3\text{D}}}, \quad (5)$$

where $M = \pi r^2 \mu_{\text{H}_2} m_{\text{H}} N_{\text{H}_2}$ is the observed gas mass M_{gas} , $\Phi = \pi r^2 B_{3\text{D}}$ is the magnetic flux, $B_{3\text{D}}$ is the three-dimensional (3D) total magnetic field strength, $(M/\Phi)_{\text{cr}} = 1/(2\pi\sqrt{G})$ is the critical mass-to-flux ratio, and G is the gravitational constant. Since the line-of-sight magnetic field strength is not constrained by polarization measurements, we estimated the 3D total magnetic field strength $B_{3\text{D}}$ from B_{pos} by adopting a statistical relation $B_{3\text{D}} \sim 1.25 B_{\text{pos}}$ (J. Liu et al. 2022b), assuming the uncertainties of factor of 2 (J. Liu et al. 2021). The factor of 1.25 is the mean value of the correlation factors derived from the statistical relation between the 3D and POS uniform magnetic field ($B_{\text{u},3\text{D}} = \frac{4}{\pi} B_{\text{u},\text{pos}}$; R. M. Crutcher et al. 2004), and the statistical relation between the 3D and POS turbulent magnetic field ($B_{\text{t},3\text{D}} = \sqrt{\frac{3}{2}} B_{\text{t},\text{pos}}$; J. Liu et al. 2021), respectively. The estimated λ values are presented in Table 3. $\lambda < 1$ indicates a magnetically subcritical state, where the magnetic field dominates over gravity and prevents gravitational collapse; $\lambda = 1$ indicates a critical state, in which the magnetic field and gravity are balanced and the system is on the verge of stability; $\lambda > 1$ denotes a magnetically supercritical state, where the magnetic field cannot overcome gravity and the system collapses. Clump 1-A, Clump 1-B, and Clump 4-A have $\lambda > 1$, suggesting that they are magnetically su-

Table 2. Physical Properties in the Two Clumps

Parameter	Clump 1-A	Clump 1-B	Clump 1-tail	Clump 4-A	Clump 4-B	Clump 4-C	Clump 4-D	Clump 4-E	Clump 4-F	Clump 4
r [pc]	0.052	0.049	0.108	0.033	0.023	0.024	0.028	0.027	0.021	0.146
F_ν [mJy]	593.4	369.5	273.6	251.1	129.6	137.4	134.6	132.2	29.5	1809.5
M_{gas} [M_\odot]	245.6	152.9	113.3	103.9	53.6	56.9	55.7	54.7	12.2	749.0
N_{H_2} [10^{23} cm $^{-2}$]	13.0	9.1	1.4	13.6	14.4	14.0	10.1	10.7	3.9	5.0
n_{H_2} [10^6 cm $^{-3}$]	6.0	4.5	0.3	10.0	15.2	14.2	8.8	9.6	4.6	0.8
σ_θ [deg] ^a	11.0 ± 0.5	22.0 ± 1.8	15.8 ± 0.9	15.0 ± 1.4	19.6 ± 2.6	35.5 ± 7.7	98.7 ± 67.1	15.1 ± 1.3	4.6 ± 0.1	-
σ_v [km s $^{-1}$]	1.68 ± 0.64	1.45 ± 0.20	2.25 ± 0.27^b	1.16 ± 0.17	1.38 ± 0.08	0.82 ± 0.12	1.03 ± 0.37	1.13 ± 0.34	0.96 ± 0.31	1.08^c

^aThe angle dispersion is derived using the regridded image (3 pixels per beam).

^bThe velocity dispersion for Clump 1-tail is derived from NH₃.

^cThe velocity dispersion for Clump 4 is derived by averaging the dispersions from all its cores.

Table 3. Magnetic Field Strengths and Properties

Parameter	Clump 1-A	Clump 1-B	Clump 1-tail ^a	Clump 4-A	Clump 4
B_{pos} [mG]	3.1	2.3	1.8	2.3	0.3
λ	2.6	2.4	0.5	3.7	9.0
\mathcal{M}_A	1.4	1.4	0.7	1.7	3.0
σ_{tot} [km s $^{-1}$]	1.70	1.47	2.27	1.19	1.11
$M_{\text{k+B}}$ [M_\odot]	179.6	123.5	-	54.7	192.4
$\alpha_{\text{k+B}}$	0.7	0.8	-	0.5	0.3

^a $M_{\text{k+B}}$ and $\alpha_{\text{k+B}}$ are not calculated for Clump 1-tail as it is an elongated diffuse structure.

percritical. Clump 1-tail has $\lambda \sim 0.5$, indicating that it is subcritical.

3.4. Alfvénic Mach Numbers

The balance between the magnetic field and turbulence can be characterized by the Alfvénic Mach number

$$\mathcal{M}_A = \sigma_{v,3D} / v_{A,3D}, \quad (6)$$

where $\sigma_{v,3D} = \sqrt{3}\sigma_v$ is the 3D velocity dispersion for isotropic turbulence, $v_{A,3D} = B_{3D}/\sqrt{\mu_0\rho}$ is the 3D Alfvénic velocity, μ_0 is the permeability of vacuum. The estimated \mathcal{M}_A values are presented in Table 3. All the cores in Clump 1 and Clump 4 have shown $\mathcal{M}_A \gtrsim 1$, suggesting that turbulence is likely play an important role in these two clumps. Clump 1-tail has a $\mathcal{M}_A \sim 0.7$, suggest that turbulence plays a less dominant role than magnetic field in this region.

3.5. Virial Parameters

To study the equilibrium states of the cores within each clump, we followed J. Liu et al. (2020) to calculate the virial parameter $\alpha_{\text{k+B}}$ by incorporating contributions from both the turbulent kinetic energy and the magnetic energy, which is given by

$$\alpha_{\text{k+B}} = \frac{M_{\text{k+B}}}{M}, \quad (7)$$

where $M_{\text{k+B}}$ is the total virial mass, including both the magnetic field virial mass and the kinetic mass, which can be estimated as

$$M_{\text{k+B}} = \sqrt{M_{\text{B}}^2 + \left(\frac{M_{\text{k}}}{2}\right)^2 + \frac{M_{\text{k}}}{2}}. \quad (8)$$

The kinetic virial mass M_{k} and magnetic field virial mass M_{B} are given by

$$M_{\text{k}} = \frac{3(5-2a)\sigma_{\text{tot}}^2 r}{(3-a)G}, \quad (9)$$

and

$$M_{\text{B}} = \frac{\pi r^2 B_{3D}}{\sqrt{\frac{3(3-a)}{2(5-2a)}\mu_0\pi G}}, \quad (10)$$

respectively, where r is the effective radius, σ_{tot} is the total gas velocity dispersion, and a is the index of the density profile $\rho(r) \propto r^{-a}$. We adopted $a = 1.6$, assuming a radial density profile (e.g., L. E. Pirogov 2009) for all cores. We estimated the total gas velocity dispersion by using $\sigma_{\text{tot}} = \sqrt{\sigma_{\text{nt}}^2 + \sigma_{\text{th}}^2}$, in which $\sigma_{\text{nt}} = \sqrt{\sigma_{\text{obs}}^2 - \frac{kT}{m_{\text{obs}}}}$ is the non-thermal velocity dispersion, and $\sigma_{\text{th}} = \sqrt{\frac{kT}{\mu_p m_{\text{H}}}}$ is the thermal velocity dispersion. Here σ_{obs} is the observed velocity dispersion, m_{obs} is the mass of the observed molecule (i.e., HN¹³C, NH₃), m_{H} is the mass of the hydrogen atom, and $\mu_p = 2.33$ is

the mean molecular weight per free particle (J. Kauffmann et al. 2008).

The values of σ_{tot} , $M_{\text{k+B}}$, and $\alpha_{\text{k+B}}$ are presented in Table 3.

4. DISCUSSION

4.1. Angular difference between multi-scale magnetic fields

In this section, we use the JCMT data (M.-Z. Yang et al. 2025), ALMA C-2 configuration data, and ALMA C-5 configuration data to compare the magnetic field structures in the Clump 1 and Clump 4 at three different resolutions: $\theta \sim 14''$ (JCMT; M.-Z. Yang et al. 2025), $\theta \sim 0''.71 \times 0''.54$ (ALMA C-2), $\theta \sim 0''.24 \times 0''.16$ (ALMA C-5). Those resolutions correspond to 0.6 pc, 5000 au, and 2000 au in linear scales, respectively. These scales in this work are referred to as the cloud-scale, the core-scale, and the condensation-scale, respectively. We iterate over each pixel to calculate the distance between all pairs of vectors from these three data sets. We then compute the absolute difference between the angles from one data set with the angles from the nearest pixels in the other data set. The inferred magnetic field orientations at multi-scales for Clump 1 and Clump 4 are shown in the Figure 2 and Figure 3, respectively.

Figure 2 (a) shows the magnetic field orientations at cloud-scale in Clump 1 aligned orderly along a northeast-southwest direction. Figure 2 (b) shows the magnetic field at core-scale. The magnetic field orientations of Clump 1-tail are consistent with those at cloud-scale, which align parallel with its major axis with a mean difference of $\sim 15^\circ$ (see Figure 4 (a)). The mean difference for all cores and Clump 1-tail between these two scales is calculated as the average value within the core masks (black contours in Figure 4) and the Clump 1-tail mask (magenta contour Figure 4). The magnetic field orientations of Clump 1-A are nearly parallel to its minor axis, which align along the east-west direction. Clump 1-B shows a similar magnetic field orientation to Clump 1-A. The magnetic field orientations of Clump 1-A and Clump 1-B at core-scale show the deviations of $\sim 35^\circ$ and $\sim 29^\circ$ from those at cloud-scale, respectively (see Figure 4 (a)). At core-scale, the magnetic field orientations transit from being perpendicular to the continuum contours in the two cores to becoming parallel to the contours in Clump 1-tail. Figures 2 (c) and (d) show that the two cores detected at core-scale are resolved into multiple compact condensations. The vectors are mostly detected from the dense regions at condensation-scale. Since the diffuse Clump 1-tail is only detected with a limited number of vectors, we only present the zoomed-in images of Clump 1-A and Clump 1-B. Figure 5 (c)

shows the histogram distributes in a right-skewed triangle distribution, which means that the orientations between these two scales are generally consistent. There are only 16% of the vectors showing an angular difference of $\geq 45^\circ$.

At the cloud-scale, the magnetic field plays a significant role in providing support against gravitational collapse (M.-Z. Yang et al. 2025). At the core-scale, the orientation in the diffuse Clump 1-tail shows consistency with the cloud-scale magnetic field orientation, as the magnetic field could effectively resist the gravitational collapse. On the other hand, the dense Clump 1-A and Clump 1-B show different orientations compared to those of the cloud-scale, as the density structures are mainly shaped by gravity in the high density regions (P. M. Koch et al. 2018). At the condensation-scale, the magnetic field orientations are predominately consistent with those at the core-scale, which suggests that gravity plays the important role in shaping the density structure in the dense regions at both scales. In addition, the sub-virial state also suggested that gravitational forces likely dominate gas dynamics at this scale. However, at condensation-scale, star formation activities (J. Liu et al. 2023) could also be a dominant force as explained in Section 4.2.

Figure 3 (a) shows that the magnetic field orientations at cloud-scale in Clump 4 primarily distribute along a north-south direction. Figure 3 (b) shows the magnetic field orientations at core-scale. Even in diffuse regions, the magnetic field is oriented in different directions. Six cores were detected, and all of them show deviations in magnetic field orientations from that at the cloud-scale, with Clump 4-A, Clump 4-B, Clump 4-C, Clump 4-D, Clump 4-E and Clump 4-F show the deviations of $\sim 31^\circ$, $\sim 30^\circ$, $\sim 42^\circ$, $\sim 48^\circ$, $\sim 16^\circ$, and $\sim 41^\circ$, respectively (see Figure 4 (b)). The discrepancies between these two scales are prominent in Clump 4 as evidenced by the binomial distribution in Figure 5 (b). Figure 3 (c)–(h) show the magnetic field at condensation-scale, which reveal that the magnetic field orientations are generally consistent between the core- and condensation-scales. The complex magnetic field orientation at the condensation-scale may be affected by the HII region nearby as shown in Figure D1 (b). However, we will not delve into this topic further in this work.

The magnetic orientation changes in Clump 4 at different scales generally follows those observed in Clump 1. Discrepancies in the magnetic field orientation occur between the cloud- and core-scales for both Clump 1 and Clump 4. This could happen when the magnetic field dominates at the cloud-scale, whereas the gravity becomes the predominant force at the core-scale. Such dis-

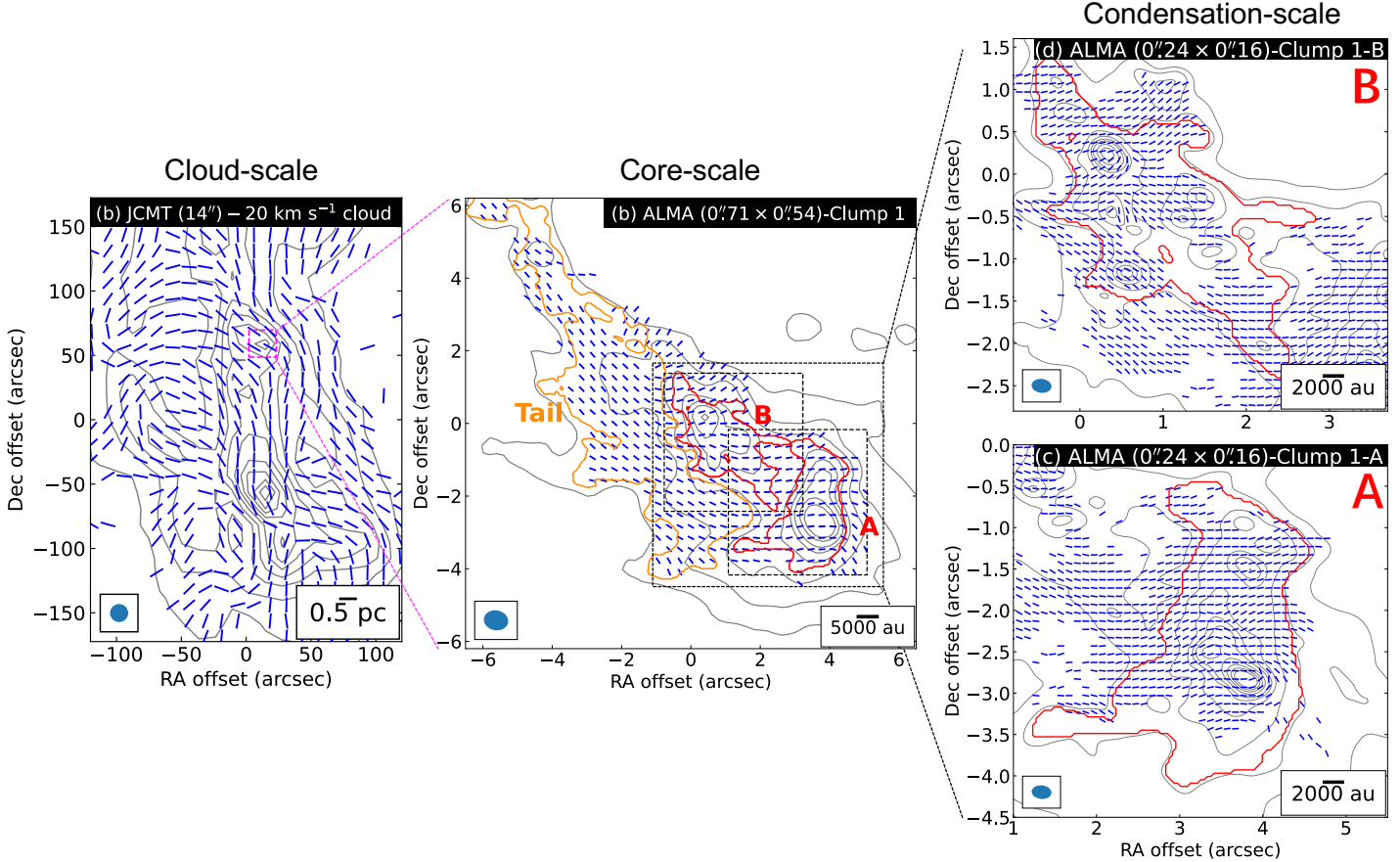


Figure 2. The inferred magnetic field orientations at multi-scales for Clump 1. The inferred magnetic field orientations (blue line segments) of Clump 1 at a resolution of $\sim 14''$ revealed by JCMT data (M.-Z. Yang et al. 2025) in panel (a). The inferred magnetic field orientations (blue line segments) of Clump 1 revealed by the ALMA C-2 configuration in panels (b) with a resolution of $\sim 0''.71 \times 0''.54$. The inferred magnetic field orientations (blue line segments) in Clump 1 revealed by the ALMA C-5 configuration in panels (c) and (d) with a resolution of $\sim 0''.24 \times 0''.17$. The synthesized beam is denoted by a filled blue ellipse at the bottom left corner in each panel. The grey contours show the Stokes I intensity in each panel. The contour levels are $[5, 25, 45, 65, 85, 105, 125, 145, 165, 185] \times \sigma$ ($\sigma = 27 \text{ mJy beam}^{-1}$) in panel (a), $[5, 25, 50, 100, 150, 200, 300, 400] \times \sigma$ ($\sigma = 0.22 \text{ mJy beam}^{-1}$) in panel (b), $[25, 50, 100, 200, 300, 400, 600, 800, 1000, 1200] \times \sigma$ ($\sigma = 32 \mu\text{Jy beam}^{-1}$) in panels (c) and (d), respectively. The vectors in panels (b), (c), and (d) are selected using super-Nyquist sampling (~ 3 pixel per beam; C. L. H. Hull et al. 2020) and set to have a uniform length.

crepancies also suggest a transition of the magnetic critical state between these two scales (J. Liu et al. 2024). In contrast, the magnetic field orientations are mostly consistent between the core- and condensation-scales for both Clump 1 and Clump 4, which could be attributed to the dominance of gravitational forces at scales smaller than 5000 au.

4.2. Relative Orientation between Magnetic Field versus Local Gravity

In this section, we follow the method introduced by J. Liu et al. (2023) to study the magnetic field and density structures in Clump 1 and Clump 4. The column density gradient and velocity gradient were derived using a 3×3

Sobel kernel (J. D. Soler et al. 2013; J. Liu et al. 2023). The local gravity gradient was derived from the column density map using the standard formula of gravity (P. M. Koch et al. 2012a; J. Liu et al. 2020). The details of calculation and uncertainty estimations can be found in J. Liu et al. (2023). The angle difference between these orientations can be characterized by the alignment measure (AM; D. F. González-Casanova & A. Lazarian 2017; A. Lazarian & K. H. Yuen 2018; J. Liu et al. 2023), which is given by

$$AM = \langle \cos(2\phi) \rangle, \quad (11)$$

where $\phi = |\theta_1 - \theta_2|$ represents the angle difference in the range of $0^\circ - 90^\circ$ between the orientations of any

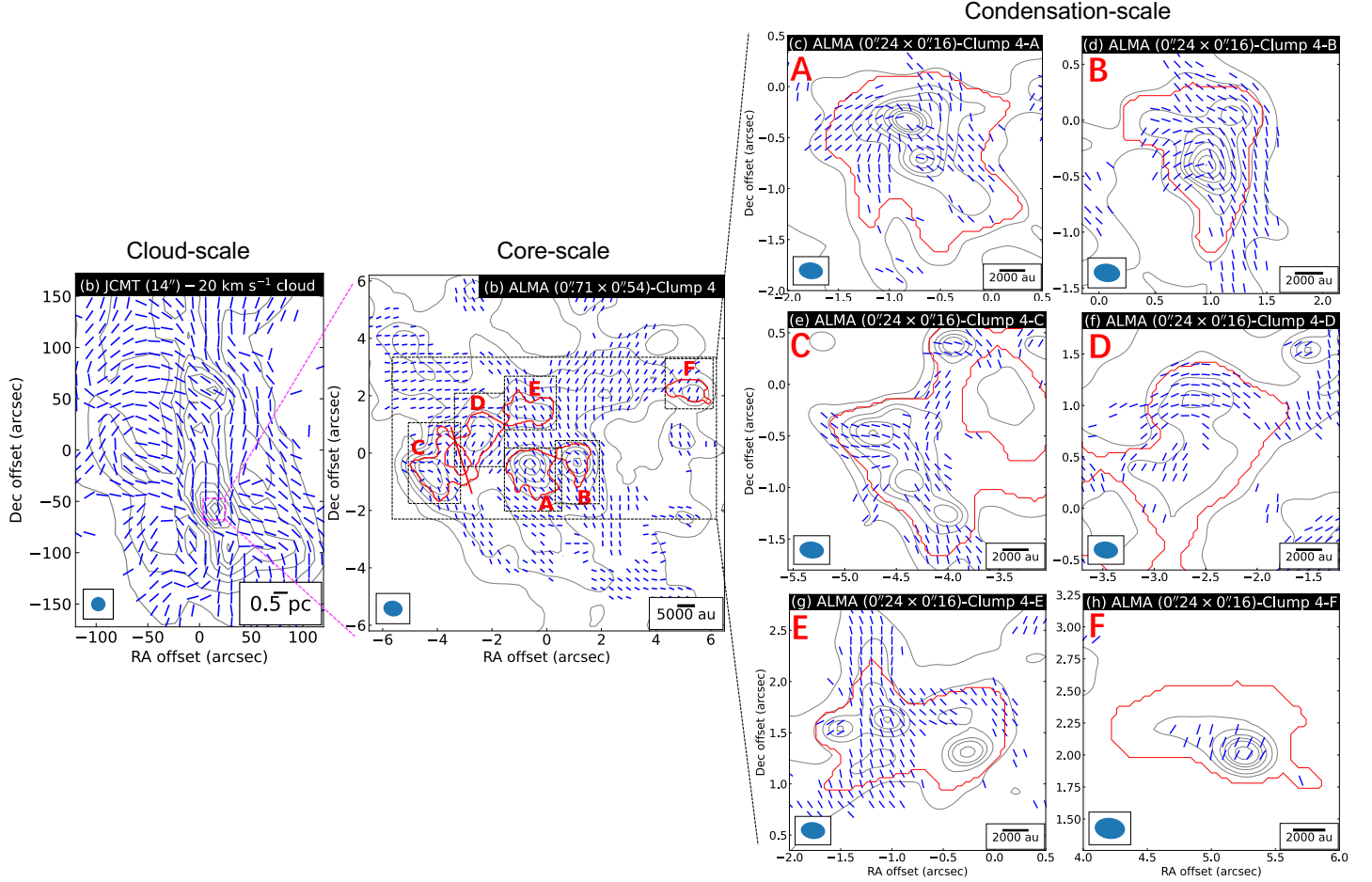


Figure 3. The inferred magnetic field orientations at multi-scales for Clump 4. The inferred magnetic field orientations (blue line segments) of Clump 4 at a resolution of $\sim 14''$ revealed by JCMT data (M.-Z. Yang et al. 2025) in panel (a). The inferred magnetic field orientations (blue line segments) in Clump 4 revealed by the ALMA C-2 configuration in panels (b) with a resolution of $\sim 0''.71 \times 0''.55$. The inferred magnetic field orientations (blue line segments) in Clump 4 revealed by the ALMA C-5 configuration in panels (c)–(h) with a resolution of $\sim 0''.24 \times 0''.16$. The synthesized beam is denoted by a filled blue ellipse at the bottom left corner in each panel. The grey contours shows the Stokes I intensity in each panel. The contour levels are $[5, 25, 45, 65, 85, 105, 125, 145, 165, 185] \times \sigma$ ($1\sigma = 27 \text{ mJy beam}^{-1}$) in panel (a), $[5, 25, 50, 100, 150, 200, 300, 400] \times \sigma$ ($1\sigma = 0.21 \text{ mJy beam}^{-1}$) in panel (b), $[50, 100, 200, 300, 400, 600, 800, 1000, 1200] \times \sigma$ ($1\sigma = 22 \mu\text{Jy beam}^{-1}$) in panels (c)–(h), respectively. The vectors in panels (b)–(h) are selected using super-Nyquist sampling (~ 3 pixel per beam; C. L. H. Hull et al. 2020) and set to have a uniform length.

two of the magnetic field (θ_B), gas column density gradient (θ_{NG}), local gravity gradient (θ_{LG}), and velocity gradient (θ_{VG}). The AM is ranged from -1 to 1 , with -1 indicating perpendicular alignment and 1 indicating parallel alignment. The AM is calculated in different N_{H_2} bins and each bin contains equal number of pixels. Each N_{H_2} bin in both Clump 1 and Clump 4 contains at least 30 independent measurements. The uncertainty of AM is estimated as $\delta\text{AM} = \sqrt{\langle\langle(\cos(2\phi))^2\rangle\rangle - \text{AM}^2 + \sum_i^n (2\sin(2\phi_i)\delta\phi_i)^2/n'}$, where n' is the number of data points, ϕ_i and $\delta\phi_i$ are the angle difference and its uncertainty, respectively,

associated with the i -th data point (J. Liu et al. 2023). Among the relative orientations (ϕ_B^{LG} , ϕ_B^{NG} , $\phi_{\text{NG}}^{\text{LG}}$, $\phi_{\text{VG}}^{\text{LG}}$, and $\phi_{\text{VG}}^{\text{NG}}$), except for ϕ_B^{LG} , all the other orientations do not show a prominent trend, and we refrain from further discussing them.

The relative orientation between the magnetic field and local gravity (ϕ_B^{LG}) quantifies the efficiency of gravity in structuring magnetic field lines and aligning them with gravitational pull (P. M. Koch et al. 2012a; J. Liu et al. 2023). The low values of ϕ_B^{LG} indicate that the magnetic field and gravity are mostly aligned with a small angular difference in orientation. In this case, the magnetic field may be ineffective at providing resistance

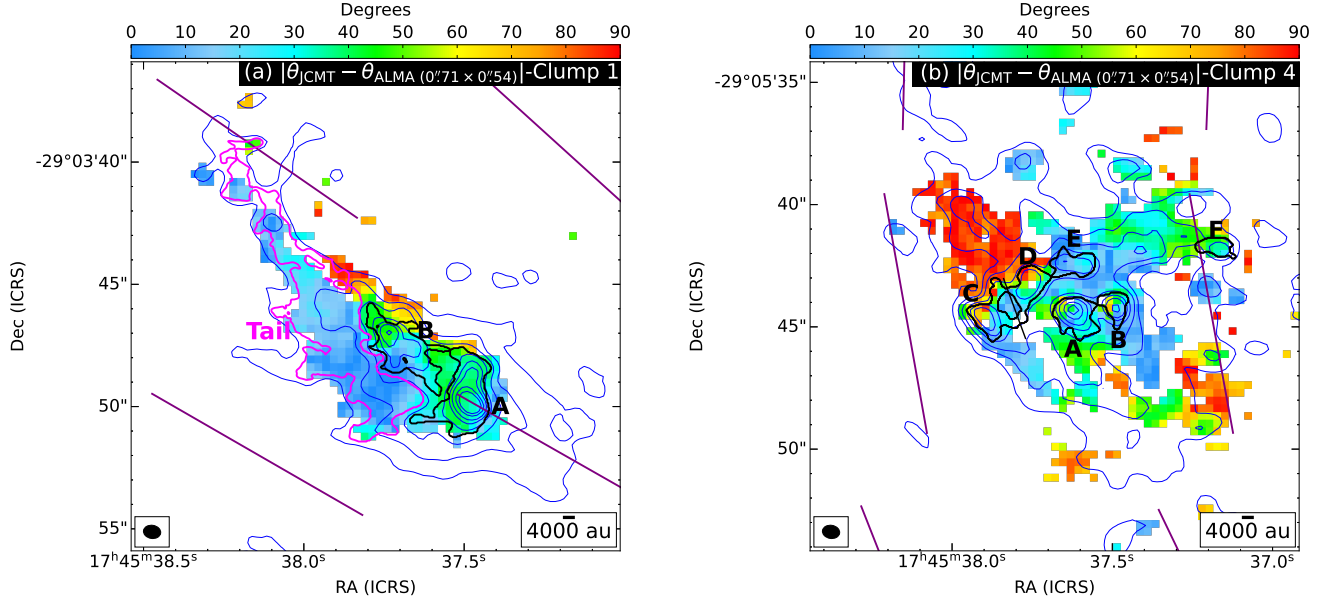


Figure 4. Absolute angular difference between the JCMT data and the ALMA C-2 configuration (resolution $\sim 0.^{\circ}71 \times 0.^{\circ}54$) data shown in color for Clump 1 and Clump 4 in panels (a) and (b), respectively. The blue contours in each panel are the Stokes I intensity from the ALMA C-2 configuration data. The blue contours in panels (a) and (b) are identical to the black contours in Figure 2 (b) and Figure 3 (b), respectively. The cores enclosed by black solid contours in these two clumps are identified by `astrodendro`, and the magenta contour in panel (a) denotes Clump 1-tail. The purple line segments in each panel show the inferred magnetic field orientation revealed by JCMT (M.-Z. Yang et al. 2025).

against gravity. The high values of ϕ_B^{LG} indicate that the magnetic field and gravity are misaligned with a large angular difference in orientation, which could allow the magnetic field to provide resistance against gravity (P. M. Koch et al. 2018). Figures 6 (a) and (b) show the spatial distribution of ϕ_B^{LG} for Clump 1 and Clump 4, respectively. Clump 1-tail shows high ϕ_B^{LG} values, while Clump 1-A and Clump 1-B show both low and high ϕ_B^{LG} values. All cores in Clump 4 show both low and high ϕ_B^{LG} values. The tangential fan-like structure observed near the peak of the continuum emission reported by P. M. Koch et al. (2018) and J. Liu et al. (2023) has also been observed toward the peaks of the condensations of Clump 1 and Clump 4. The areas of the fan-like structures showing low ϕ_B^{LG} values suggest that gravitational collapse can occur without much of magnetic resistance (P. M. Koch et al. 2018; J. Liu et al. 2023), where the magnetic field acts as a channel to transfer materials (P. M. Koch et al. 2018). The Clump 1-tail shows mostly the high ϕ_B^{LG} values close to 90° , which indicates a predominantly perpendicular alignment. The perpendicular alignment observed in Clump 1-tail suggests a strong resistance of magnetic field against gravity in the diffuse region, where densities are low and no condensations are identified (P. M. Koch et al. 2018).

Figure 7 (a) shows that the AM_B^{LG} values in both the entire clump and the cores of Clump 1 suggest a random alignment. The random alignments suggest a trans-critical state or the distortions of magnetic field may arise from sources other than gravity. This is because gravity-induced distortions typically show as parallel alignments instead of the random alignments (e.g., P. M. Koch et al. 2018; Q. Zhang et al. 2025). The potential sources contributing to the random alignments may include star formation activities such as outflows and converging flows (J. Liu et al. 2023).

Figure 7 (b) shows that the AM_B^{LG} values for Clump 4 generally increase with increasing N_{H_2} , which suggests that a preferentially more perpendicular alignment transits to a random alignment. The alignments suggest that magnetic field could work effectively in Clump 4-F, whereas Clump 4-D is overwhelmed by the gravity without much resistance from magnetic field (P. M. Koch et al. 2018). The gravity likely dominates the Clump 4-B and Clump 4-E with small contribution from magnetic field or star formation activities. The alignments in Clump 4-A and Clump 4-C suggest that magnetic field could work effectively with some impact from the star formation activities (J. Liu et al. 2023). Overall, in both clumps, the alignment we observed is inconsistent with the preferentially parallel configuration observed

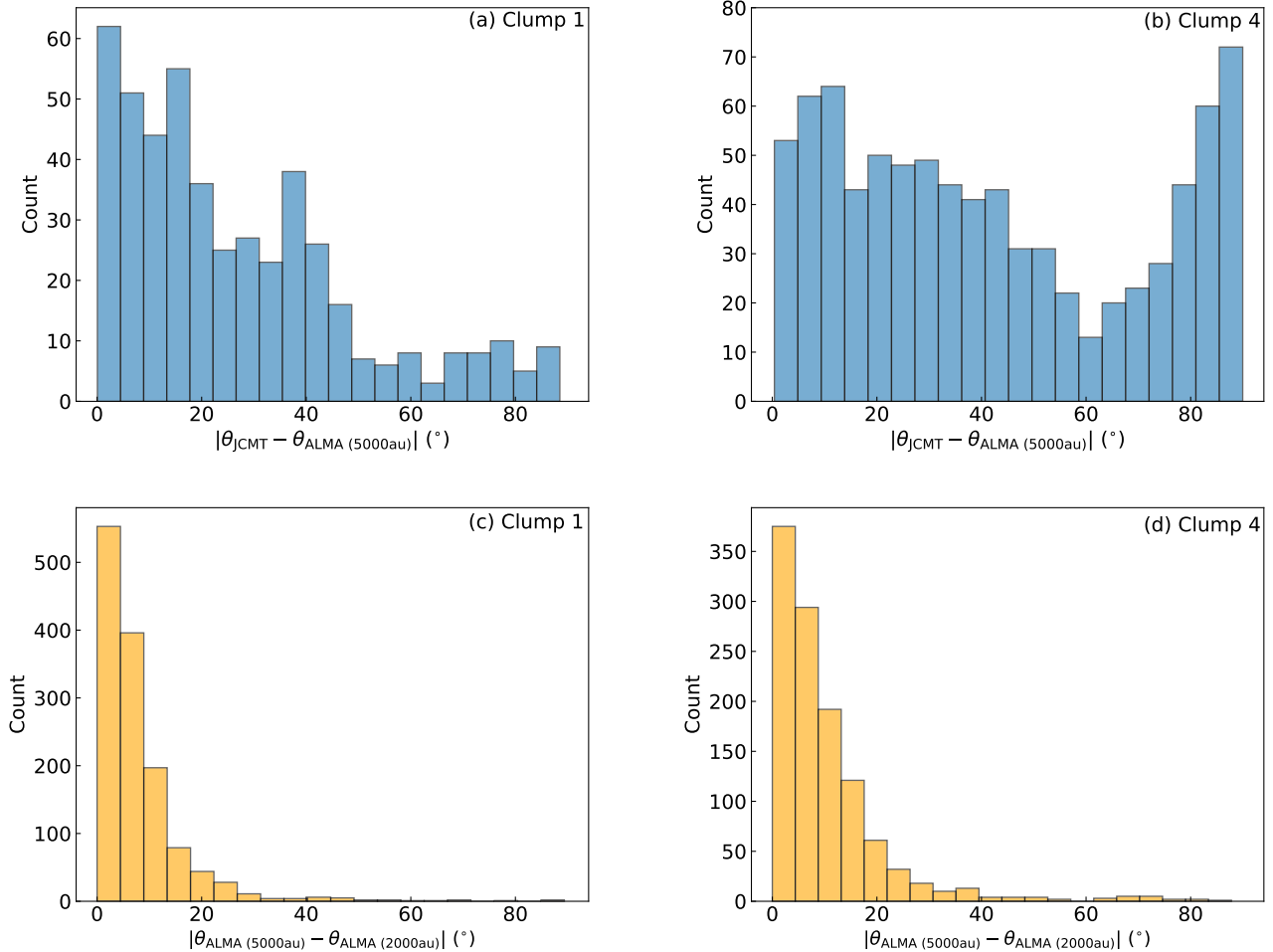


Figure 5. Top panels: Histogram of the absolute angular difference between the JCMT data and the ALMA C-2 configuration (resolution ~ 5000 au) for Clump 1 and Clump 4 in panels (a) and (b), respectively. Bottom panels: Histogram of the absolute angular difference between the ALMA C-2 (resolution ~ 5000 au) and C-5 configurations (resolution ~ 2000 au) for Clump 1 and Clump 4 in panels (c) and (d), respectively.

across the CMZ (X. Pan et al. 2025). It is also inconsistent with the alignment observed toward the 17 massive protostellar cluster-forming clumps in the Galactic disk, where the magnetic field and column density show parallel alignment at higher column densities (Q. Zhang et al. 2025). The former suggests that most dense gas structures in the CMZ are stable against gravitational collapse, supported by strong turbulence and magnetic fields (X. Pan et al. 2025). The latter indicates that gravitational collapse occurs on envelope scales as the magnetic field is dragged inward by infalling motions in magnetically supercritical gas (Q. Zhang et al. 2025). In contrast, our results showing a random alignment suggest that these two clumps are predominantly transcritical, or that the magnetic field is significantly influenced by star formation feedback (J. Liu et al. 2023).

4.3. Magnetic tension force (F_B) versus the Gravitational force (F_G) between the cores

We quantitatively compare the magnetic field tension force F_B and the gravitational force F_G between the cores (inter-core) as shown in Figure 8 for Clump 1 and Clump 4, respectively. By using the KTH method (P. M. Koch et al. 2012a), the magnetic field tension force is described as $F_B = B^2/(4\pi R) = (\sqrt{\Sigma_B(\rho\nabla\Psi)4\pi R})^2/(4\pi R) = \Sigma_B\rho\nabla\Psi$, in which Σ_B is defined as $\Sigma_B = (F_B/|F_G|)_{\text{local}} = \sin\phi_{\text{LG}}^{\text{NG}}/\sin(90^\circ - \phi_B^{\text{NG}})$ (P. M. Koch et al. 2012a,b), and the gravitational force is $F_G = \rho\nabla\Psi$, if the hydrostatic dust pressure force is negligible. Here, $\rho = \mu_{\text{H}_2}m_{\text{H}}n_{\text{H}_2}$ is the gas density, and $\nabla\Psi$ is the gradient of gravitational potential. The direction of F_G is calculated from $\nabla\Psi$. The direction of F_B is determined by first tracing the magnetic field lines based on the rotated polarization vectors, followed

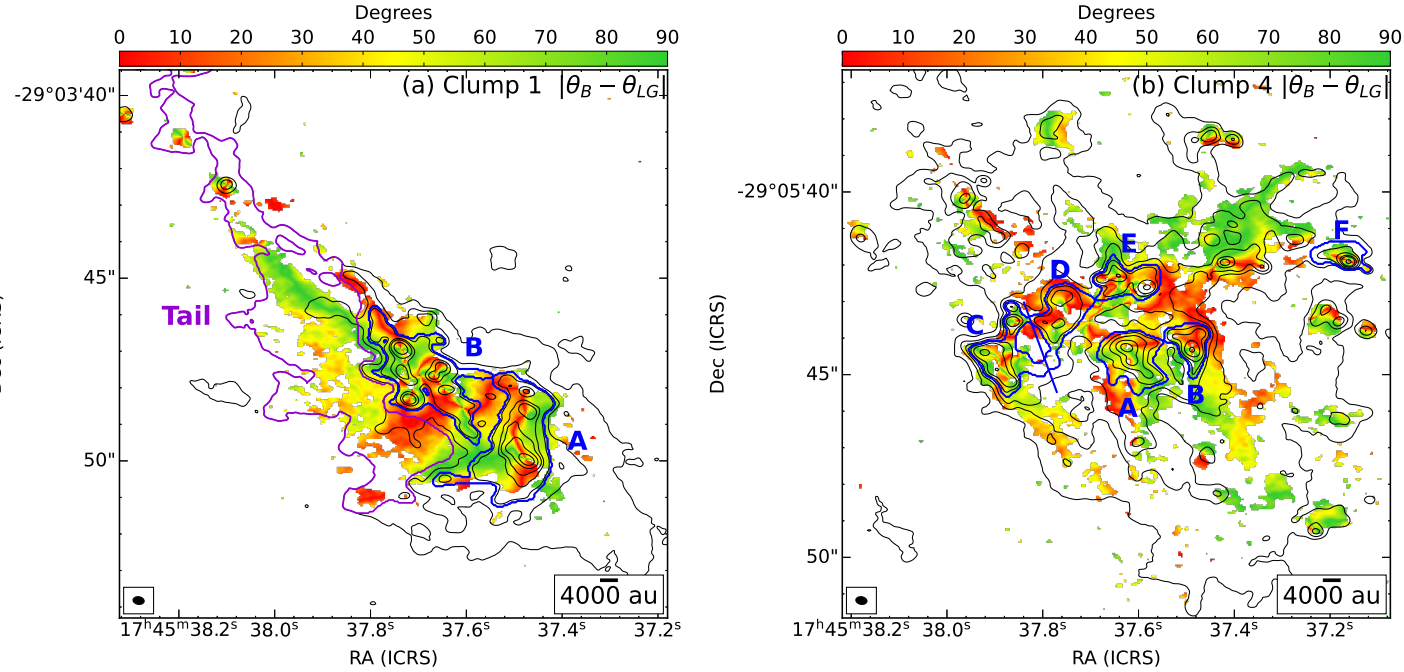


Figure 6. Relative orientation between the inferred magnetic field (θ_B) and local gravity (θ_{LG}) in color overlaid with the Stokes I emission in black contours. The black contours are $[5, 25, 50, 100, 175, 350, 700] \times \sigma$ ($1\sigma = 65 \mu\text{Jy beam}^{-1}$) in panel (a) and $[5, 25, 50, 100, 150, 300, 600] \times \sigma$ ($1\sigma = 48 \mu\text{Jy beam}^{-1}$) in panel (b). The cores enclosed by blue solid contours in these two clumps are identified by `astrodendro`, and purple contour in panel (a) denotes Clump 1-tail. The synthesized beam size is denoted by the filled black ellipse in the bottom left corner.

by a 90 degree rotation toward the concave side of the curved field lines (P. M. Koch et al. 2012a). In general, the greater the curvature, the stronger the magnetic tension force. If the vectors are mostly aligned, it indicates little to no curvature, and the direction of the magnetic tension force becomes undefined (the pixels with undefined direction were masked out). Finally, we project the magnitude and direction of the forces within the inter-core along the direction toward the mass centroids of the cores. For each inter-core between a pair of cores, the force vectors are projected toward one core at a time. The negative values of F_B/F_G indicate that the two forces act in opposite directions, whereas the positive values indicate that they act in the same direction.

The left and right panels of Figure 8 show the same inter-cores projected onto the centroid mass of different cores. Figure 8(a) and (c) show that the F_B/F_G ratios for the inter-cores toward Clump 1-A and Clump 4-A mostly fall within the range of -1 to 1 , indicating that F_B is generally comparable to or weaker than F_G toward these two cores. On the other hand, Figure 8(b) and (d) show that more pixels in the inter-cores have F_B/F_G in the range of -2 to -1 toward Clump 1-B and Clump 4-B, suggesting a stronger F_B acting in the opposition of F_G . Consequently, the gas is more likely to infall to-

ward the centers of Clump 1-A and Clump 4-A. We note that Clump 1-A and Clump 4-A are more massive than Clump 1-B and Clump 4-B. Thus, in the inter-cores, the magnetic field may provide some support against gravity, but it is insufficient to prevent gas from infalling toward the cores, particularly towards the more massive cores.

4.4. Equilibrium States and Star Formation Activities of the Cores

All the cores in Clump 1 and Clump 4 have shown $\alpha_{k+B} \lesssim 1$, which suggest that these cores are gravitationally bound. Clump 1-A and Clump 1-B have shown $\alpha_{k+B} \sim 1$, which means that these two cores are approaching a nearly quasi-equilibrium state (J. Liu et al. 2024), suggesting that the gravitation collapse is likely balanced by magnetic field and other supporting forces. Clump 4 shows the relatively low values of $\alpha_{k+B} \sim 0.3$, suggesting a sub-virial state where the gravitational force likely dominates gas dynamics in these cores. Clump 1-A, Clump 1-B, and Clump 4-A show $\lambda > 1$ and $\mathcal{M}_A > 1$, suggesting that both gravity and turbulence could shape the physical properties of these cores. For the diffuse Clump 1-tail, both λ and \mathcal{M}_A are smaller than 1. This could indicate that the magnetic field is

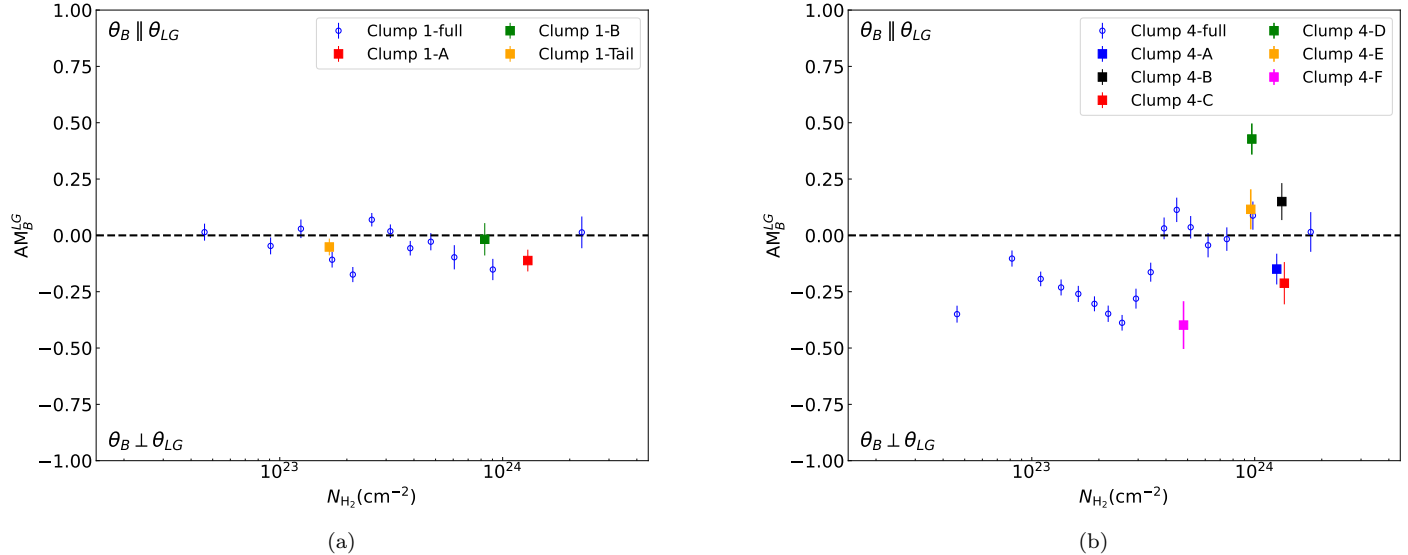


Figure 7. Relative orientations between θ_B and θ_{LG} for (a) Clump 1 and (b) Clump 4. The empty blue circles denote N_{H_2} bins obtain for the whole clump and they are divided to 12 bins for (a) Clump 1 and 18 bins (b) Clump 4 (> 30 independent measurements in each bin) in each plot. Different cores in each plot are color-coded with squares. Each core and tail in Clump 1 is divided into 1 N_{H_2} bins (> 45 independent measurements in each bin). Each core in Clump 4 is divided into 1 N_{H_2} bins (> 6 independent measurements in each bin). The black dashed line at $AM = 0$ denotes the random alignment. $AM > 0$ is defined as the parallel alignment, and $AM < 0$ is defined as the perpendicular alignment.

dominant over both turbulence and gravity, probably preventing the gas from collapsing to form cores.

Both H_2O masers and outflows are clearly detected toward Clump 1-A, Clump 1-B, Clump 4-A, Clump 4-B and Clump 4-C (X. Lu et al. 2019a,b, 2021), along with the derived $\alpha_{k+B} < 1$ (sub-virial), indicating ongoing star formation activities in these cores. There is no H_2O maser and outflow identified in Clump 4-D (X. Lu et al. 2019a,b, 2021). The sub-virial state and the predominantly parallel alignment of AM_B^{LG} suggest Clump 4-D might reach the pre-collapse or the early collapse phase, yet star formation has not begun. Clump 4-E has shown signatures of star formation, because it is in a sub-virial state with outflow detection, although there is no maser detection toward this core (X. Lu et al. 2019b,a, 2021). Oppositely, Clump 4-F was only detected in H_2O maser without outflow detection. Moreover, the AM_B^{LG} shows the predominantly perpendicular alignment, which suggests a strong resistance of magnetic field against gravity. Therefore, there is no clear sign indicating star formation activities in Clump 4-F despite the H_2O maser.

5. CONCLUSIONS

We present the results of ALMA dust polarization observations to show the magnetic field structures of Clump 1 and Clump 4 in the 20 km s^{-1} cloud. In addition, we also study the multi-scale magnetic fields with the JCMT polarization data (M.-Z. Yang et al. 2025). The results are summarized as follows.

1. We have divided both Clump 1 and Clump 4 into multiple cores using `astrodendro`, and Clump 1-tail is an additional diffuse substructure enclosed at 5σ level in Clump 1. The magnetic field strengths derived using the ADF method range from 0.3–3.1 mG. The normalized mass-to-flux ratios λ for the cores in Clump 1 and Clump 4 (except for Clump 1-tail) are $\lambda > 1$, suggesting that these cores are mostly magnetically supercritical, where gravity dominates over magnetic support, while Clump 1-tail is in the subcritical state, in which magnetic support overcome the gravity. All the cores in Clump 1 and Clump 4 have shown $\alpha_{k+B} \lesssim 1$, which suggest that these cores are likely gravitationally bound. All the cores in Clump 1 and Clump 4 are super-Alvénic ($\mathcal{M}_A \gtrsim 1$), while Clump 1-tail sub-Alvénic ($\mathcal{M}_A \sim 0.7$), suggesting that turbulence plays a more important role than magnetic field in the dense cores and a less dominant role in the diffuse region.
2. We study the angular difference between multi-scale magnetic fields probed by JCMT and ALMA. The results suggest that the cloud-scale (0.6 pc) and core-scale (5000 au) magnetic fields show angular deviations, with the primary difference arising from the dense cores. At the cloud-scale, the magnetic field predominates, while gravity becomes the dominant force at the core-scale.

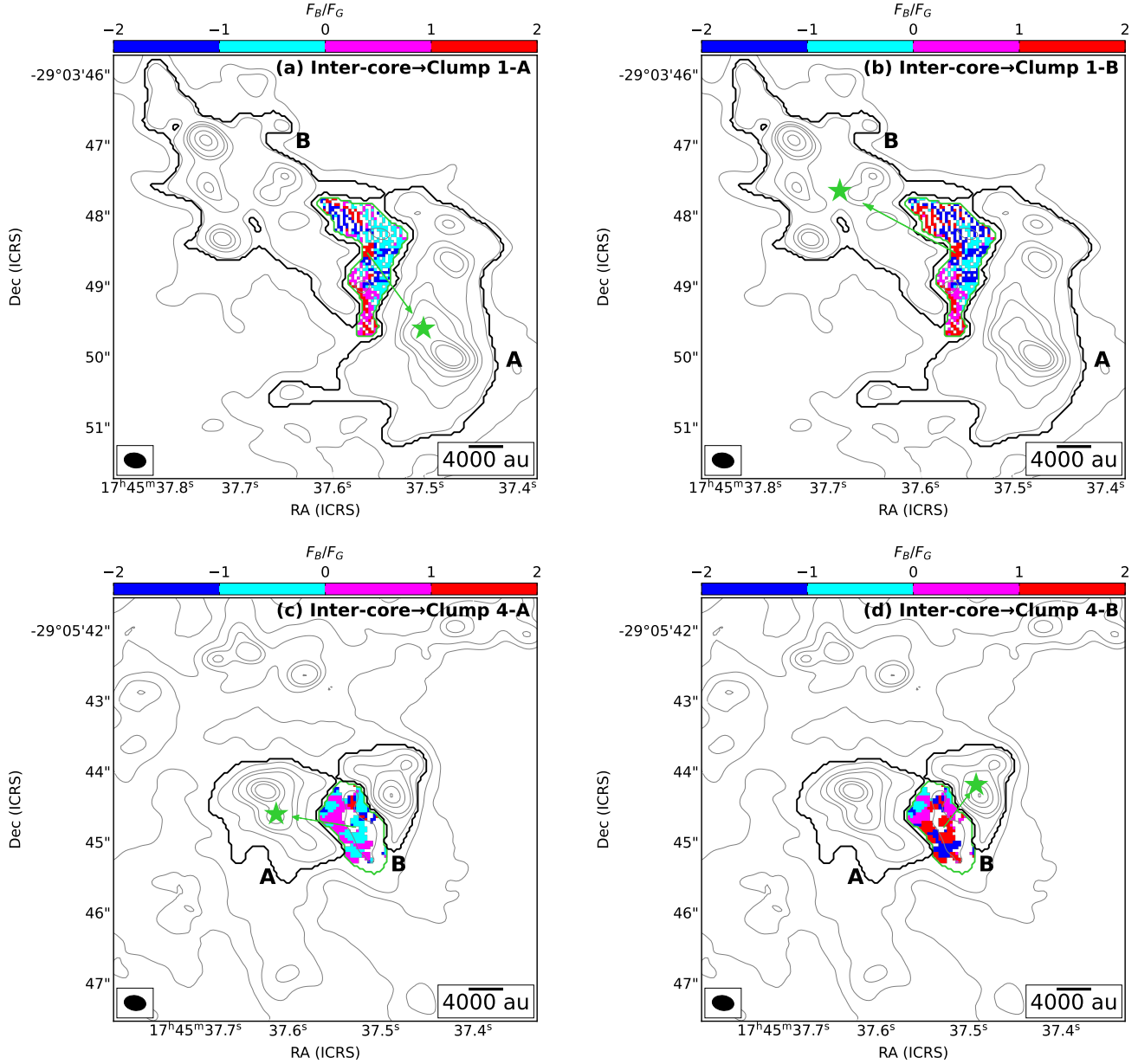


Figure 8. Top: F_B/F_G ratios for the inter-core in Clump 1 (color). The gray contours are the Stokes I emission, and the contour levels are $[25, 50, 100, 150, 200, 350, 500, 650] \times \sigma$ ($1\sigma = 65 \mu\text{Jy beam}^{-1}$). Bottom: The F_B/F_G ratios for the inter-core in Clump 4 (color). The gray contours are the Stokes I emission, and the contour levels are $[25, 50, 100, 150, 200, 350, 500, 650] \times \sigma$ ($1\sigma = 48 \mu\text{Jy beam}^{-1}$). For all panels, the black solid contours indicate the cores, the green solid contours define the inter-cores. The green stars within the cores denote their positions of mass centroids. The green arrows indicate the projection directions of the ratio of the two forces.

The magnetic field orientations are largely consistent between the core-scale and condensation-scale (2000 au), indicating that both are predominantly governed by gravity.

3. The relative orientation between the magnetic field and local gravity (ϕ_B^{LG}) suggest a strong resistance of magnetic field against gravity in the dif-

fuse Clump 1-tail. The magnetic field of the dense cores is likely affected by gravity and star formation activities.

4. The ratio of the magnetic field tension force F_B to the gravitational force F_G for inter-cores in Clump 1 and Clump 4 suggests that the magnetic field may provide some support against gravity,

but it is insufficient to prevent gas from infalling toward the cores.

ACKNOWLEDGMENTS

We thank the referee for the thorough review and for providing the helpful and detailed comments. This work has been supported by the Natural Science Foundation of Shanghai (No. 23ZR1482100), the Strategic Priority Research Program of the Chinese Academy of Sciences (CAS) Grant No. XDB0800300, the National Natural Science Foundation of China (NSFC) through grant Nos. 12273090 and 12322305, the National Key R&D Program of China (No. 2022YFA1603101), and the CAS “Light of West China” Program No. xbgz-zdsys-

202212. This paper makes use of the following ALMA data: ADS/JAO.ALMA#2021.1.00286.S. ALMA is a partnership of ESO (representing its member states), NSF (USA), and NINS (Japan), together with NRC (Canada), MOST and ASIAA (Taiwan), and KASI (Republic of Korea), in cooperation with the Republic of Chile. The Joint ALMA Observatory is operated by ESO, AUI/NRAO, and NAOJ.

Facilities: ALMA

Software: astropy (Astropy Collaboration et al. 2013), APLpy (T. Robitaille & E. Bressert 2012), CASA (CASA Team et al. 2022), matplotlib (J. D. Hunter 2007), astrodendro (E. W. Rosolowsky et al. 2008)

REFERENCES

Andersson, B. G., Lazarian, A., & Vaillancourt, J. E. 2015, *ARA&A*, 53, 501, doi: [10.1146/annurev-astro-082214-122414](https://doi.org/10.1146/annurev-astro-082214-122414)

Ao, Y., Henkel, C., Menten, K. M., et al. 2013, *A&A*, 550, A135, doi: [10.1051/0004-6361/201220096](https://doi.org/10.1051/0004-6361/201220096)

Astropy Collaboration, Robitaille, T. P., Tollerud, E. J., et al. 2013, *A&A*, 558, A33, doi: [10.1051/0004-6361/201322068](https://doi.org/10.1051/0004-6361/201322068)

Bally, J., Stark, A. A., Wilson, R. W., & Henkel, C. 1987, *ApJS*, 65, 13, doi: [10.1086/191217](https://doi.org/10.1086/191217)

Barnes, A. T., Longmore, S. N., Battersby, C., et al. 2017, *MNRAS*, 469, 2263, doi: [10.1093/mnras/stx941](https://doi.org/10.1093/mnras/stx941)

Battersby, C., Walker, D. L., Barnes, A., et al. 2024, arXiv e-prints, arXiv:2410.17334, doi: [10.48550/arXiv.2410.17334](https://doi.org/10.48550/arXiv.2410.17334)

Battersby, C., Walker, D. L., Barnes, A., et al. 2025, *ApJ*, 984, 156, doi: [10.3847/1538-4357/adb5f0](https://doi.org/10.3847/1538-4357/adb5f0)

CASA Team, Bean, B., Bhatnagar, S., et al. 2022, *PASP*, 134, 114501, doi: [10.1088/1538-3873/ac9642](https://doi.org/10.1088/1538-3873/ac9642)

Chapin, E. L., Berry, D. S., Gibb, A. G., et al. 2013, *MNRAS*, 430, 2545, doi: [10.1093/mnras/stt052](https://doi.org/10.1093/mnras/stt052)

Crutcher, R. M., Nutter, D. J., Ward-Thompson, D., & Kirk, J. M. 2004, *ApJ*, 600, 279, doi: [10.1086/379705](https://doi.org/10.1086/379705)

Dahmen, G., Huttemeister, S., Wilson, T. L., & Mauersberger, R. 1998, *A&A*, 331, 959, doi: [10.48550/arXiv.astro-ph/9711117](https://doi.org/10.48550/arXiv.astro-ph/9711117)

Dempsey, J. T., Friberg, P., Jenness, T., et al. 2013, *MNRAS*, 430, 2534, doi: [10.1093/mnras/stt090](https://doi.org/10.1093/mnras/stt090)

Federrath, C., Rathborne, J. M., Longmore, S. N., et al. 2016, *ApJ*, 832, 143, doi: [10.3847/0004-637X/832/2/143](https://doi.org/10.3847/0004-637X/832/2/143)

Ferrière, K., Gillard, W., & Jean, P. 2007, *A&A*, 467, 611, doi: [10.1051/0004-6361:20066992](https://doi.org/10.1051/0004-6361:20066992)

Ginsburg, A., Henkel, C., Ao, Y., et al. 2016, *A&A*, 586, A50, doi: [10.1051/0004-6361/201526100](https://doi.org/10.1051/0004-6361/201526100)

González-Casanova, D. F., & Lazarian, A. 2017, *ApJ*, 835, 41, doi: [10.3847/1538-4357/835/1/41](https://doi.org/10.3847/1538-4357/835/1/41)

GRAVITY Collaboration, Abuter, R., Aimar, N., et al. 2022, *A&A*, 657, A82, doi: [10.1051/0004-6361/202142459](https://doi.org/10.1051/0004-6361/202142459)

Henshaw, J. D., Barnes, A. T., Battersby, C., et al. 2023, in Astronomical Society of the Pacific Conference Series, Vol. 534, Protostars and Planets VII, ed. S. Inutsuka, Y. Aikawa, T. Muto, K. Tomida, & M. Tamura, 83, doi: [10.48550/arXiv.2203.11223](https://doi.org/10.48550/arXiv.2203.11223)

Henshaw, J. D., Longmore, S. N., Kruijssen, J. M. D., et al. 2016, *MNRAS*, 457, 2675, doi: [10.1093/mnras/stw121](https://doi.org/10.1093/mnras/stw121)

Heywood, I., Rammala, I., Camilo, F., et al. 2022, *ApJ*, 925, 165, doi: [10.3847/1538-4357/ac449a](https://doi.org/10.3847/1538-4357/ac449a)

Hildebrand, R. H. 1988, *QJRAS*, 29, 327

Hildebrand, R. H., Kirby, L., Dotson, J. L., Houde, M., & Vaillancourt, J. E. 2009, *ApJ*, 696, 567, doi: [10.1088/0004-637X/696/1/567](https://doi.org/10.1088/0004-637X/696/1/567)

Houde, M., Hull, C. L. H., Plambeck, R. L., Vaillancourt, J. E., & Hildebrand, R. H. 2016, *ApJ*, 820, 38, doi: [10.3847/0004-637X/820/1/38](https://doi.org/10.3847/0004-637X/820/1/38)

Houde, M., Vaillancourt, J. E., Hildebrand, R. H., Chitsazzadeh, S., & Kirby, L. 2009, *ApJ*, 706, 1504, doi: [10.1088/0004-637X/706/2/1504](https://doi.org/10.1088/0004-637X/706/2/1504)

Hull, C. L. H., Cortes, P. C., Gouellec, V. J. M. L., et al. 2020, *PASP*, 132, 094501, doi: [10.1088/1538-3873/ab99cd](https://doi.org/10.1088/1538-3873/ab99cd)

Hunter, J. D. 2007, *Computing in Science and Engineering*, 9, 90, doi: [10.1109/MCSE.2007.55](https://doi.org/10.1109/MCSE.2007.55)

Immer, K., Kauffmann, J., Pillai, T., Ginsburg, A., & Menten, K. M. 2016, *A&A*, 595, A94, doi: [10.1051/0004-6361/201628777](https://doi.org/10.1051/0004-6361/201628777)

Karoly, J., Ward-Thompson, D., Pattle, K., et al. 2025, ApJL, 982, L22, doi: [10.3847/2041-8213/adbc67](https://doi.org/10.3847/2041-8213/adbc67)

Kauffmann, J., Bertoldi, F., Bourke, T. L., Evans, N. J., I., & Lee, C. W. 2008, A&A, 487, 993, doi: [10.1051/0004-6361:200809481](https://doi.org/10.1051/0004-6361:200809481)

Kauffmann, J., Pillai, T., Zhang, Q., et al. 2017, A&A, 603, A89, doi: [10.1051/0004-6361/201628088](https://doi.org/10.1051/0004-6361/201628088)

Koch, P. M., Tang, Y.-W., & Ho, P. T. P. 2012a, ApJ, 747, 79, doi: [10.1088/0004-637X/747/1/79](https://doi.org/10.1088/0004-637X/747/1/79)

Koch, P. M., Tang, Y.-W., & Ho, P. T. P. 2012b, ApJ, 747, 80, doi: [10.1088/0004-637X/747/1/80](https://doi.org/10.1088/0004-637X/747/1/80)

Koch, P. M., Tang, Y.-W., Ho, P. T. P., et al. 2018, ApJ, 855, 39, doi: [10.3847/1538-4357/aaa4c1](https://doi.org/10.3847/1538-4357/aaa4c1)

Krieger, N., Ott, J., Beuther, H., et al. 2017, ApJ, 850, 77, doi: [10.3847/1538-4357/aa951c](https://doi.org/10.3847/1538-4357/aa951c)

Kruijssen, J. M. D., Longmore, S. N., Elmegreen, B. G., et al. 2014, MNRAS, 440, 3370, doi: [10.1093/mnras/stu494](https://doi.org/10.1093/mnras/stu494)

Lazarian, A., & Yuen, K. H. 2018, ApJ, 853, 96, doi: [10.3847/1538-4357/aaa241](https://doi.org/10.3847/1538-4357/aaa241)

Liu, J., Qiu, K., & Zhang, Q. 2022a, ApJ, 925, 30, doi: [10.3847/1538-4357/ac3911](https://doi.org/10.3847/1538-4357/ac3911)

Liu, J., Zhang, Q., Commerçon, B., et al. 2021, ApJ, 919, 79, doi: [10.3847/1538-4357/ac0cec](https://doi.org/10.3847/1538-4357/ac0cec)

Liu, J., Zhang, Q., & Qiu, K. 2022b, Frontiers in Astronomy and Space Sciences, 9, 943556, doi: [10.3389/fspas.2022.943556](https://doi.org/10.3389/fspas.2022.943556)

Liu, J., Zhang, Q., Qiu, K., et al. 2020, ApJ, 895, 142, doi: [10.3847/1538-4357/ab9087](https://doi.org/10.3847/1538-4357/ab9087)

Liu, J., Zhang, Q., Koch, P. M., et al. 2023, ApJ, 945, 160, doi: [10.3847/1538-4357/acb540](https://doi.org/10.3847/1538-4357/acb540)

Liu, J., Zhang, Q., Lin, Y., et al. 2024, ApJ, 966, 120, doi: [10.3847/1538-4357/ad3105](https://doi.org/10.3847/1538-4357/ad3105)

Longmore, S. N., Bally, J., Testi, L., et al. 2013, MNRAS, 429, 987, doi: [10.1093/mnras/sts376](https://doi.org/10.1093/mnras/sts376)

Lu, X., Zhang, Q., Kauffmann, J., et al. 2015, ApJL, 814, L18, doi: [10.1088/2041-8205/814/2/L18](https://doi.org/10.1088/2041-8205/814/2/L18)

Lu, X., Zhang, Q., Kauffmann, J., et al. 2017, ApJ, 839, 1, doi: [10.3847/1538-4357/aa67f7](https://doi.org/10.3847/1538-4357/aa67f7)

Lu, X., Mills, E. A. C., Ginsburg, A., et al. 2019a, ApJS, 244, 35, doi: [10.3847/1538-4365/ab4258](https://doi.org/10.3847/1538-4365/ab4258)

Lu, X., Zhang, Q., Kauffmann, J., et al. 2019b, ApJ, 872, 171, doi: [10.3847/1538-4357/ab017d](https://doi.org/10.3847/1538-4357/ab017d)

Lu, X., Li, S., Ginsburg, A., et al. 2021, ApJ, 909, 177, doi: [10.3847/1538-4357/abde3c](https://doi.org/10.3847/1538-4357/abde3c)

Lu, X., Liu, J., Pillai, T., et al. 2024, ApJ, 962, 39, doi: [10.3847/1538-4357/ad1395](https://doi.org/10.3847/1538-4357/ad1395)

Mangilli, A., Aumont, J., Bernard, J. P., et al. 2019, A&A, 630, A74, doi: [10.1051/0004-6361/201935072](https://doi.org/10.1051/0004-6361/201935072)

Morris, M., & Serabyn, E. 1996, ARA&A, 34, 645, doi: [10.1146/annurev.astro.34.1.645](https://doi.org/10.1146/annurev.astro.34.1.645)

Ossenkopf, V., & Henning, T. 1994, A&A, 291, 943

Pan, X., Zhang, Q., Qiu, K., et al. 2024, ApJ, 972, 30, doi: [10.3847/1538-4357/ad5aea](https://doi.org/10.3847/1538-4357/ad5aea)

Pan, X., Zhang, Q., Qiu, K., et al. 2025, ApJ, 991, 156, doi: [10.3847/1538-4357/adf8c7](https://doi.org/10.3847/1538-4357/adf8c7)

Paré, D. M., Chuss, D. T., Karpovich, K., et al. 2025, ApJ, 978, 28, doi: [10.3847/1538-4357/ad9586](https://doi.org/10.3847/1538-4357/ad9586)

Pierce-Price, D., Richer, J. S., Greaves, J. S., et al. 2000, ApJL, 545, L121, doi: [10.1086/317884](https://doi.org/10.1086/317884)

Pillai, T., Kauffmann, J., Tan, J. C., et al. 2015, ApJ, 799, 74, doi: [10.1088/0004-637X/799/1/74](https://doi.org/10.1088/0004-637X/799/1/74)

Pirogov, L. E. 2009, Astronomy Reports, 53, 1127, doi: [10.1134/S1063772909120051](https://doi.org/10.1134/S1063772909120051)

Robitaille, T., & Bressert, E. 2012, APLpy: Astronomical Plotting Library in Python, Astrophysics Source Code Library, record ascl:1208.017

Robitaille, T., Rice, T., Beaumont, C., et al. 2019, astrodendro: Astronomical data dendrogram creator, Astrophysics Source Code Library, record ascl:1907.016 <http://ascl.net/1907.016>

Rosolowsky, E. W., Pineda, J. E., Kauffmann, J., & Goodman, A. A. 2008, ApJ, 679, 1338, doi: [10.1086/587685](https://doi.org/10.1086/587685)

Soler, J. D., Hennebelle, P., Martin, P. G., et al. 2013, ApJ, 774, 128, doi: [10.1088/0004-637X/774/2/128](https://doi.org/10.1088/0004-637X/774/2/128)

Stolovy, S., Ramirez, S., Arendt, R. G., et al. 2006, in Journal of Physics Conference Series, Vol. 54, Journal of Physics Conference Series, ed. R. Schödel, G. C. Bower, M. P. Munoz, S. Nayakshin, & T. Ott (IOP), 176–182, doi: [10.1088/1742-6596/54/1/030](https://doi.org/10.1088/1742-6596/54/1/030)

Tang, Y., Wang, Q. D., Wilson, G. W., et al. 2021, MNRAS, 505, 2392, doi: [10.1093/mnras/stab1191](https://doi.org/10.1093/mnras/stab1191)

Ward-Thompson, D., Pattle, K., Bastien, P., et al. 2017, ApJ, 842, 66, doi: [10.3847/1538-4357/aa70a0](https://doi.org/10.3847/1538-4357/aa70a0)

Yang, M.-Z., Lai, S.-P., Karoly, J., et al. 2025, ApJ, 983, 184, doi: [10.3847/1538-4357/adbe34](https://doi.org/10.3847/1538-4357/adbe34)

Zhang, Q., Liu, J., Zeng, L., et al. 2025, ApJ, 992, 103, doi: [10.3847/1538-4357/adf9cb](https://doi.org/10.3847/1538-4357/adf9cb)

APPENDIX

A. DENDROGRAM PARAMETERS

To better analyze the physical and the magnetic field properties, we divided each clump into cores using the `astrodendro` Python package (T. Robitaille et al. 2019; E. W. Rosolowsky et al. 2008). The cores were identified as branches, which represent the intermediate structures that can split into smaller branches or leaves in the hierarchical structures of the dendrogram. When applying `astrodendro`, the minimum value (`min_value`) was set to 10σ , the minimum significance for structures (`min_delta`) was set at 200σ , and the minimum number of pixels (`min_npix`) that required for a substructure was set to 35 pixels, which is equivalent to the number of pixels inside one beam. The `min_delta` was set sufficiently high to avoid leaves (with no further substructures in the hierarchy) from being classified as cores. This parameter setup for core identification was determined through trial and error to ensure consistency with the ALMA C-2 configuration data at the core-scale (~ 5000 au; see Section 4.1). Additionally, we manually enclosed the northeastern side of the Clump 1 at 5σ to study the morphology of the diffuse emission and named it as Clump 1-tail as shown in Figure 1 (b). The condensations were identified as the isolated compact structures within each core.

B. VELOCITY DISPERSION AND ANGLE DISPERSION

Figure B1 shows the velocity dispersion for Clump 1 and Clump 4 obtained by performing Gaussian fittings. When choosing the molecular line to derive the velocity dispersion, we selected a line with a critical density that is more or less comparable to the density of the measured region. For instance, for the diffuse region such as the Clump 1-tail, we used the NH₃ ($J, K = 3, 3$) line from Karl G. Jansky Very Large Array (JVLA) observations (X. Lu et al. 2017), and for the relatively dense cores, we used the HN¹³C ($J = 4-3$) line from the same ALMA observations of this work but excluding the QA-semipass data to derive the velocity dispersion. The velocity dispersion was calculated by first performing a Gaussian fit to each pixel individually within all the cores and Clump 1-tail, then taking the average of the standard deviations across all pixels within each core and Clump 1-tail as the dispersion value. Figure B2 shows the polarization position angle distributions for the entire Clump 1 and Clump 4. Figure B3 shows the polarization position angle distributions for the cores within each clump. The polarization angle dispersions are obtain by performing the Gaussian fittings of the angle distributions.

C. MAGNETIC FIELD STRENGTH ESTIMATION WITH ADF METHOD

The ADF method improves upon the Davis–Chandrasekhar–Fermi (DCF) method in the angular dispersion estimation by taking into account of the ordered field contribution, observational effects, and line-of-sight signal averaging (R. H. Hildebrand et al. 2009; M. Houde et al. 2009, 2016). The ADF shown in Figure C1 is given by M. Houde et al. (2016):

$$1 - \langle \cos[\Delta\Phi(l)] \rangle \simeq a_2 l^2 + \frac{\langle B_0^2 \rangle}{\langle B_t^2 \rangle} C \times \left\{ \frac{1}{C_1} [1 - e^{-l^2/2(\delta^2 + 2W_1^2)}] + \frac{1}{C_2} [1 - e^{-l^2/2(\delta^2 + 2W_2^2)}] - \frac{1}{C_{12}} [1 - e^{-l^2/2(\delta^2 + W_1^2 + W_2^2)}] \right\}, \quad (C1)$$

where $\Delta\Phi(l)$ is the angular difference of two magnetic field vectors at a separation of distance l , $a_2 l^2$ is the second-order term of the Taylor expansion for the ordered field, δ is the turbulent correlation length, B_t is the turbulent magnetic field, B_0 is the ordered magnetic field, W_1 is the geometric mean of FWHM of the synthesized beam size divided by $\sqrt{8 \ln 2}$, and W_2 accounts for the large-scale filter effect obtained by using the maximum recoverable scale divided by $\sqrt{8 \ln 2}$. C is the coefficient, which is given by M. Houde et al. (2016):

$$C_1 = \frac{(\delta^2 + 2W_1^2)}{\sqrt{2\pi}\delta^3}, \quad (C2)$$

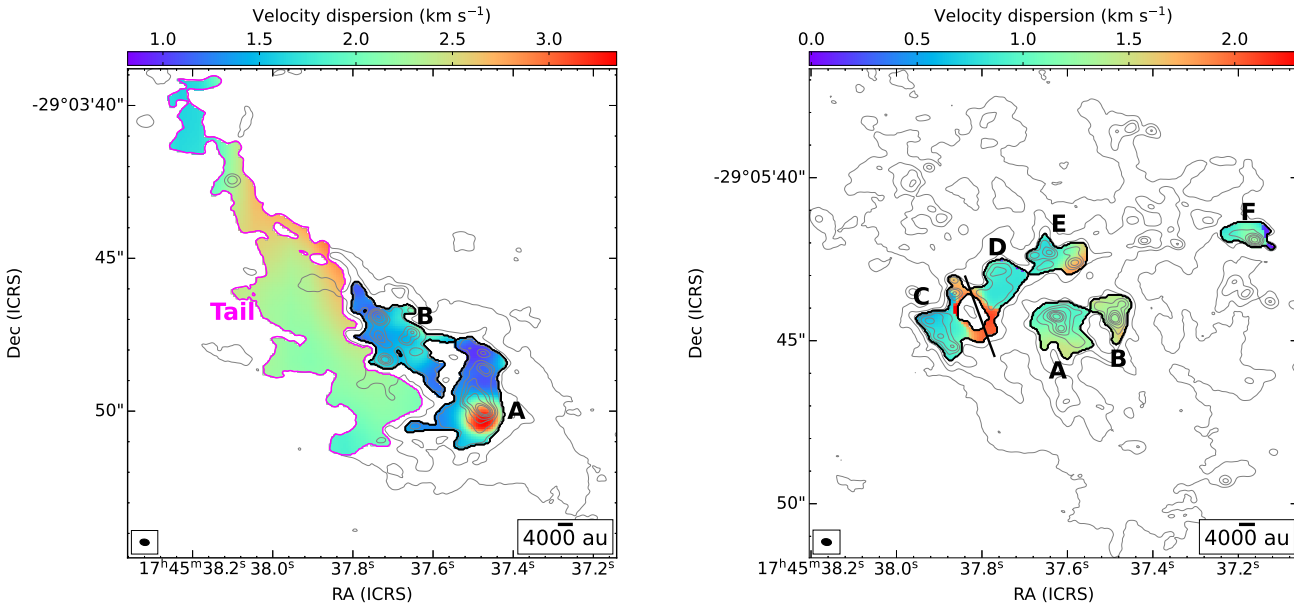


Figure B1. Left panel: The color shows the velocity dispersions for Clump 1-A and Clump 1-B estimated using the HN¹³C ($J = 4-3$) emission and for Clump 1-tail estimated using the NH₃ emission. The grey contours are the Stokes I and the contour levels in both panels are identical to Figure 1 (b). Right panel: The color shows the velocity dispersions for Clump 4 estimated using the HC₃N emission. The grey contours are the Stokes I and the contour levels are identical to Figure 1 (c). The cores enclosed by black solid contours in both panels are identified by `astrodendro`, and the magenta contour in left panel denotes Clump 1-tail.

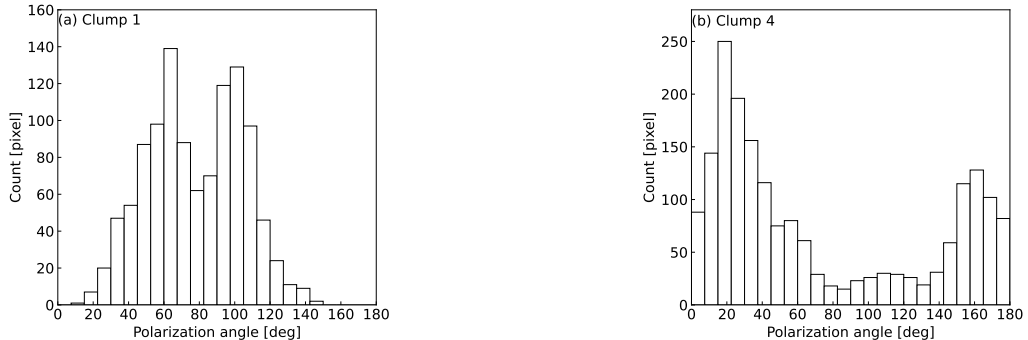


Figure B2. Histograms of the polarization position angles for the Clump 1 and Clump 4. The polarization position angles are measured from north toward east.

$$C_2 = \frac{(\delta^2 + 2W_2^2)}{\sqrt{2\pi}\delta^3}, \quad (C3)$$

$$C_{12} = \frac{(\delta^2 + W_1^2 + W_2^2)}{\sqrt{2\pi}\delta^3}, \quad (C4)$$

and

$$C = \left(\frac{1}{C_1} + \frac{1}{C_2} - \frac{2}{C_{12}} \right)^{-1}. \quad (C5)$$

The turbulent-to-total field strength ratio $\langle B_t^2 \rangle / \langle B^2 \rangle$ is given by J. Liu et al. (2021):

$$\langle B_t^2 \rangle / \langle B^2 \rangle = \frac{\langle B_t^2 \rangle / \langle B_0^2 \rangle}{1 + (\langle B_t^2 \rangle / \langle B_0^2 \rangle)}. \quad (C6)$$

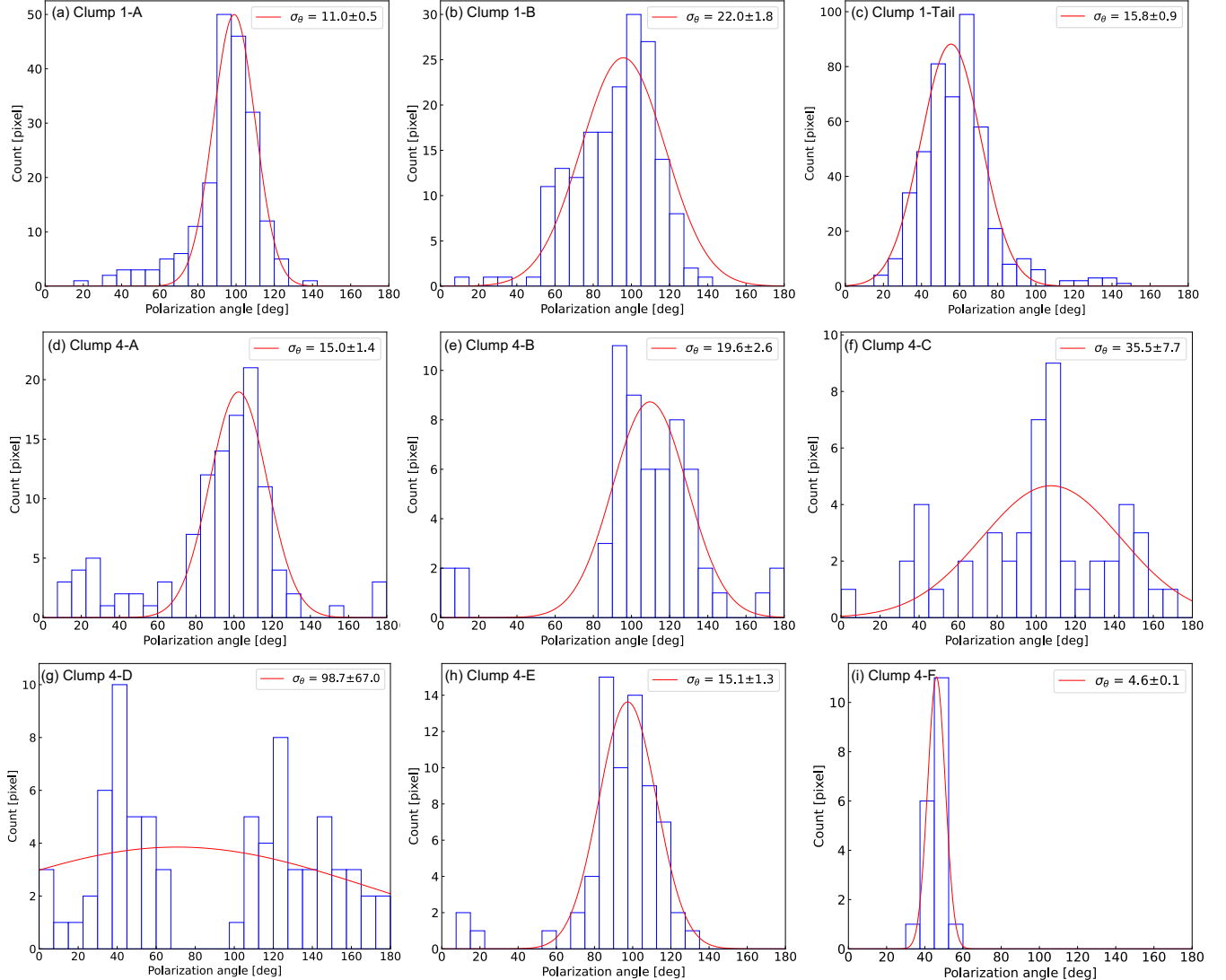


Figure B3. Histograms of the polarization position angles for the cores of Clump 1 and Clump 4. The polarization position angles are measured from north toward east. The red curve denotes the Gaussian fitting line in each panel.

D. VLA C-BAND CONTINUUM IMAGE

Previous study has shown that the magnetic field structures in the CMZ are likely affected by its physical environments such as HII regions (X. Lu et al. 2024). Key findings include the identification of the cometary magnetic field in Sgr C possibly due to the cloud interaction with an expanding HII region, and the curved magnetic field in the Dust Ridge possibly tracing converging gas flows (X. Lu et al. 2024).

X. Lu et al. (2015) and X. Lu et al. (2017) have studied an HII region in Clump 4 as shown in Figure D1 (b). The magnetic field in Clump 4-C across the 3σ contour of the HII region shows an orthogonal orientation. The vectors in Clump 4-C on the western side of the 3σ contour show a curvature structure along the contour line.

There is no detection of HII regions toward Clump 1 (Figure D1 (a)). However, several filaments (narrowly elongated structure shown in blueish color) are observed toward Clump 1. The magnetic field orientation in Clump 1-tail deviates from long axis of the filaments, which is partially consistent with the findings of D. M. Paré et al. (2025), who reported a perpendicular alignment between the magnetic field and the filament.

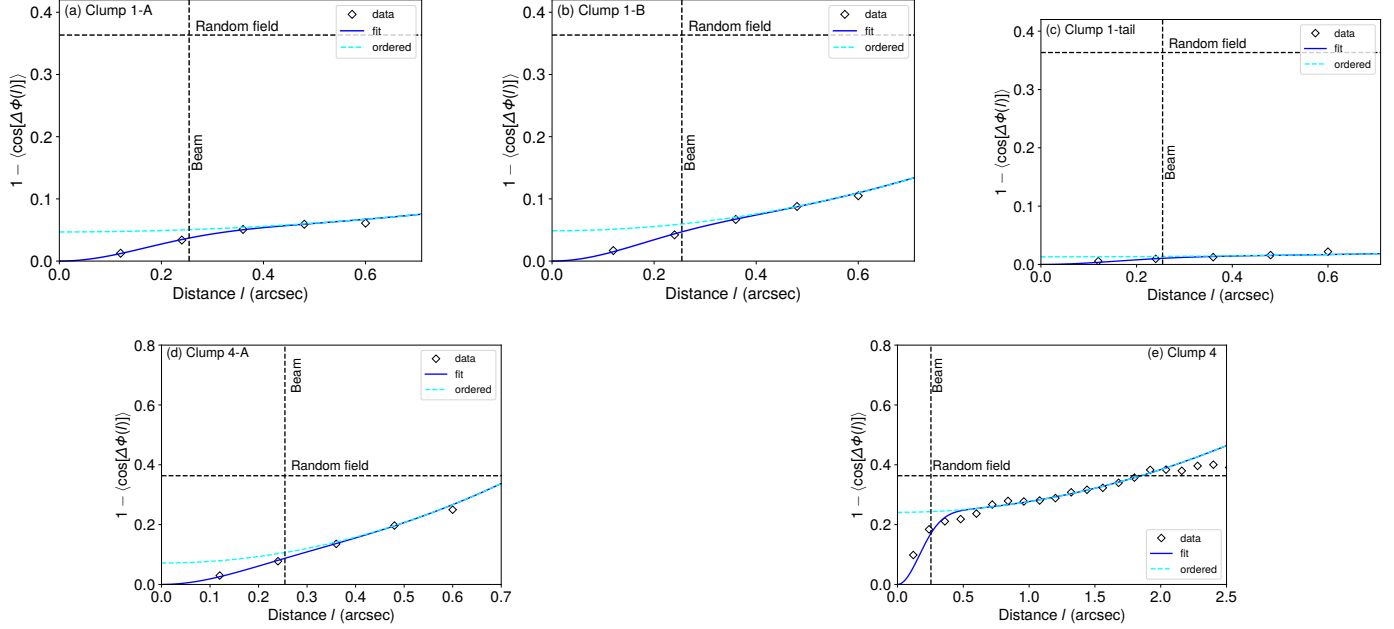


Figure C1. The angular dispersion function (ADF) $1 - \langle \cos[\Delta\Phi(l)] \rangle$ (in diamonds) is plotted as a function of the distance (l). The blue line shows the correlated turbulent component of the best fit. The cyan labels within the plots indicate the ordered component due to the synthesized beam. The vertical black dashed line shows the synthesized beam size. The horizontal dashed line shows the ADF value corresponding to a random field (J. Liu et al. 2021).

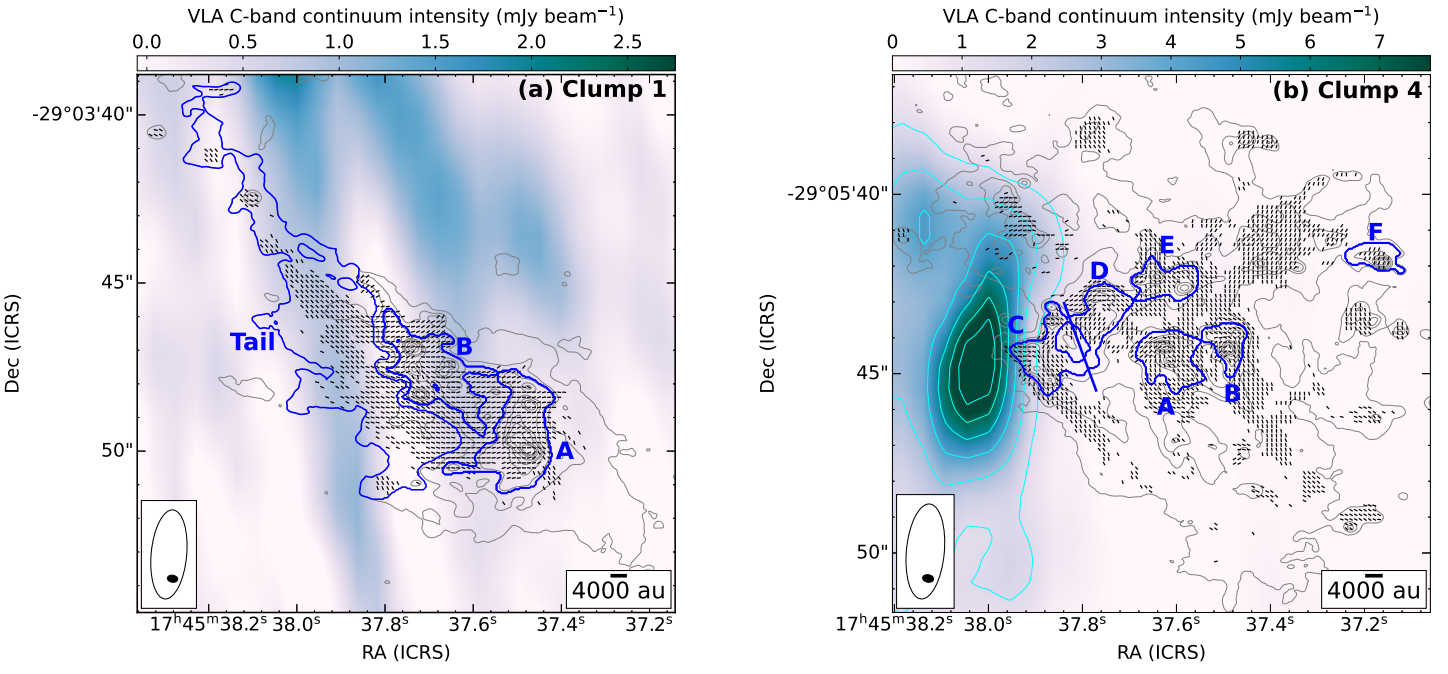


Figure D1. VLA C-band continuum emission (X. Lu et al. 2019a) in color and cyan contours overlaid with the ALMA 870 μm Stokes I emission (this work) in gray contours and the inferred magnetic field orientations (this work) in black line segments for (a) Clump 1 and (b) Clump 4, respectively. The gray contour levels and black vectors in panels (a) and (b) are identical to those in the Figure 1. The cyan contour levels in panel (b) are $[5, 10, 15, 20, 25, 30] \times \sigma$ ($1\sigma = 0.28 \text{ Jy beam}^{-1}$). The blue contours in panels (a) and (b) denote the cores identified by `astrodendro` and Clump 1-tail. The synthesized beams for VLA and ALMA are denoted by the open ellipse and the black dot at the bottom left corner in each panel.

